Electrical Properties of $BaZr_{0.1}Ce_{0.7}Y_{0.1}Yb_{0.1}O_{3-\delta}$ and its application in Intermediate Temperature Solid Oxide Fuel Cells

A Thesis
Presented to
The Academic Faculty

by

Benjamin H. Rainwater

In Partial Fulfillment
of the Requirements for the Degree
Master of Science in the
School of Materials Science and Engineering

Georgia Institute of Technology
August 2012

Electrical Properties of $BaZr_{0.1}Ce_{0.7}Y_{0.1}Yb_{0.1}O_{3-\delta}$ and its application in Intermediate Temperature Solid Oxide Fuel Cells

Approved by:

Dr. Meilin Liu, Advisor
School of Materials Science and Engineering
Georgia Institute of Technology

Dr. Preet Singh
School of Materials Science and Engineering
Georgia Institute of Technology

Dr. Joe Cochran
School of Materials Science and Engineering
Georgia Institute of Technology

Date Approved: June 18, 2012

ACKNOWLEDGEMENTS

The research from which this thesis was written would not have been started or carried to completion without the support and guidance of so many. I am especially grateful for my advisor, Dr. Meilin Liu. His guidance allowed me to quickly find meaningful and original research topics during my education at Georgia Tech. The research environment that he provided made readily available all the expertise and equipment necessary for my research. The cohesive internationality of his research group sparked unique discussions and independent study about topics both near and far from science and engineering, which made the research experience richer. I am also grateful to Dr. Mingfei Liu for his guidance and daily consultation throughout the course of my research. From his knowledge of solid oxide fuel cells, world-class fabrication techniques, and the common experimental methods used in the work, he provided invaluable instruction and expertise.

I would like to thank Dr. Joe Cochran and Dr. Preet Singh for their willingness to serve on my thesis committee and for their contributions to my thesis.

I am grateful for the constant communication I have had with my parents and brothers throughout my time at Georgia Tech. Their listening ears and words of advice helped me to process and relate thoughts and ideas that stemmed from my work.

This research was supported by the National Science Foundation under Grant No. DGE-1148903 and by the HetroFoaM Center, an Energy Frontier Research Center funded by the U.S. Department of Energy, Office of Science, Office of Basic Energy Sciences under Award Number DE-SC0001061.

Ben Rainwater

June 2012, Atlanta, GA, USA

TABLE OF CONTENTS

LIST OF TABLES

LIST OF FIGURES

LIST OF SYMBOLS

a	activity
C_k	concentration (mol cm^{-3}) of species k
d	diameter (cm)
e	elementary charge (coulomb)
E_a	activation energy
E_N	Nernst Potential (V)
E^O	standard potential (V)
F	Faraday's Constant (C/mol)
$\Delta^r G$	gibbs free energy of the reaction
$\Delta^r H$	reaction enthalpy
k	reaction rate constant
L	pellet thickness (cm)
N_A	Avogadro's number
$\dot{n}_{el}$	molar flow of electrons (mol/s)
$\dot{n}_{H_2}$	molar flow of fuel mol/s)
$\dot{n}_{H_2O,\ O\ (anode)}$	molar flow of water at the anode outlet (mol/s)
$\dot{n}_{H_2O,\ O\ (cathode)}$	molar flow of water at the cathode outlet (mol/s)
P^I_K	partial pressure of species k in compartment I
P^{II}_K	partial pressure of species k in compartment II
PH_2	hydrogen partial pressure
PH_2O	water partial pressure

PO_2	oxygen partial pressure
R	universal gas constant (J K^{-1} mol^{-1})
R_b	bulk resistance (Ω)
S	pellet cross-sectional area (cm^2)
$\Delta^r S$	reaction entropy
T	absolute temperature, K
t_k	transference number of species k
$U_{f\,H2}$	fuel utilization rate
$V_O^{\cdot\cdot}$	oxygen vacancy
$Y_{H_2,\,O}$	molar concentration of the total molar flow at the anode outlet, I
$Y_{H_2,\,I}$	molar concentration of the total molar flow at the anode outlet, O
z_k	charge of species k
η_{anode}	anode polarization (V)
$\eta_{cathode}$	cathode polarization (V)
η^{el}	quantity of released electrons related to the utilized fuel
$\eta_{electrolyte}$	electrolyte polarization (V)
η_{thermo}	thermodynamic conversion efficiency
σ	bulk conductivity(S/cm)
σ_O	constant (y-intercept of ln(σT) vs. 1/T))
$\nabla\varphi$	electrical potential gradient (V)

LIST OF ABBREVIATIONS

BET	Brunauer, Emmett, and Teller Theory
BZCYYb	$BaZr_{0.1}Ce_{0.7}Y_{0.1}Yb_{0.1}O_{3-\delta}$
BZCY	Yttria doped Barium Cerate - Barium Zirconate Solid Solution
BCY	Yttria doped Barium Cerate
BZY	Yttria doped Barium Zirconate
EES	Electrical Energy Storage
EIS	Electrochemical Impedance Spectroscopy
emf	Electromotive Force
GDC	Gadolinium doped Ceria
IT-SOFC	Intermediate Temperature Solid Oxide Fuel Cells
LSCF	$La_{0.6}Sr_{0.4}Co_{0.2}Fe_{0.8}O_{3-\delta}$
MCFC	Molten Carbonate Fuel Cell
NETL	National Energy Technology Laboratory
OCV	open circuit voltage
PAFC	Phosphoric Acid Fuel Cell
PEM	Proton Exchange Membrane
PLD	Pulsed Laser Deposition
PZT	lead zirconate titanate
SECA	Solid State Energy Conversion Alliance
SEM	Scanning Electron Microscopy
SOFC	Solid Oxide Fuel Cell
SSR	Solid State Reaction

TEC	Thermal Expansion Coefficient
TGA	Thermal Gravimetric Analysis
TPB	Triple Phase Boundary
XAFS	X-Ray Absorption Fine Structure
XRD	X-Ray Diffraction
YSZ	Yttria-stabilized Zirconia

SUMMARY

The scarcity of fossil fuels, the increase in greenhouse gases levels, and the expected rapid growth of energy consumption in the upcoming years urges the development of renewable and efficient energy conversion technologies. Solid oxide fuel cells (SOFCs) convert chemical fuels directly to electricity more efficiently and cleanly than traditional conversion methods. SOFCs have not been widely commercialized due to the high operating temperature of conventional oxygen anion conducting yttria-stabilized zirconia (YSZ) based systems. SOFCs based on proton conducting ceramics, however, can operate at lower temperatures than conventional YSZ based systems due to low activation energy for protonic defect transport when compared to oxygen vacancy transport. Lower operating temperatures ease the critical materials requirements of fuel cell system components, reduce costs, and prolong system lifetimes. Proton conducting fuel cells also generate cell reaction products on the cathode side, leaving the fuel pure and increasing the theoretical efficiency of the cell. Because of this, work has been done to understand the fundamental properties of intermediate temperature, proton conducting oxides for use in solid oxide fuel cells.

$BaCeO_3$-based perovskite materials are candidates for use in IT-SOFCs when doped with trivalent cations in the B-site. B-site doping forms oxygen vacancies which greatly increases the conductivity of the material. The oxygen vacancies are consumed during the creation of protonic defects or electronic defects, depending on the atmosphere and temperature range. Dopant size affects the symmetry of the perovskite structure. The symmetry and the chemical nature of the dopant effects both oxygen anion and protonic transport which affects the total conductivity of the system. Because each trivalent B-site dopant uniquely affects the $BaCeO_3$-based system,

experimental work must be done to determine the structure and electrical conductivity of each doped $BaCeO_3$-based system and to distinguish the charge carriers of each doped $BaCeO_3$-based system in specific atmospheres and at specific temperatures. The Y^{3+} and Yb^{3+} doped $BaCeO_3$-based system, $BaZr_{0.1}Ce_{0.7}Y_{0.1}Yb_{0.1}O_{3-\delta}$ (BZCYYb), was recently reported for use in IT-SOFCs. SOFCs based on BZCYYb displayed high performance and unique tolerances to sulfur and carbon containing environments when BZCYYb was used as the ion conducting phase of the nickel cermet anode. While the BZCYYb perovskite has been used successfully in SOFC systems, a more basic understanding of the BZCYYb structure, electrical conductivity, and the portion of the charge carried by each charge carrier under fuel cell conditions has not been reported.

In this work, the BZCYYb material is fabricated by the solid state reaction method and characterized by SEM and HT-XRD. A NiO-BZCYYb mixture is also fabricated and analyzed due to the importance of the mixture after fuel cell component processing. The total conductivity of BZCYYb in H_2/H_2O, O_2/H_2O, and air atmospheres in the IT-SOFC temperature range is reported. The activation energy for transport at these conditions is determined from the conductivity data and the transference numbers of protonic defects, oxygen anion defects and electronic defects in the BZCYYb material are determined by the concentration cell - OCV method. BZCYYb is a mixed proton, oxygen anion, and electronic conductor at IT-SOFC temperature ranges (450^oC – 750^oC), in H_2, O_2, and H_2O containing atmospheres and is predominately a proton conductor under anode conditions and predominately an oxygen anion conductor under cathode conditions.

A better understanding of the conductivity and charge carriers clarifies the feasibility of using BZCYYb in each component of the fuel cell system as well as in other electrochemical

devices. Ni-BZCYYb/BZCYYb/BZCYYb-LSCF fuel cells were constructed and peak power densities of ~1.2 W/cm^2 were reported at 750^{o}C after optimization of the Ni-BZCYYb anode porosity. Decreasing the Ni-BZCYYb anode porosity did not significantly affect the electrical conductivity of the anode, however the peak power densities of the IT-SOFCs based on the anode with less porosity, calculated from I-V curve data, showed dramatic improvement. The fuel cell with the lowest anode porosity demonstrated the highest performance. This finding is in stark contrast to the optimal anode porosity needed for high performance in YSZ-based, oxygen anion conducting SOFCs. Because of significant proton conduction in the BZCYYb material, fuel cell reaction products (water) form at the cathode side and less porosity is required on the anode side. The improvement in performance in the BZCYYb based IT-SOFC is attributed to the unique microstructure formed in the Ni-BZCYYb anode when no pore forming additives are used. The unique microstructure may contribute to high electrocatalytic behavior for anode reactions. This work provides a new understanding for the rational development of high performance, intermediate temperature SOFCs based on proton-conducting electrolytes.

CHAPTER 1

INTRODUCTION

1.1 Energy Conversion Issues

Awareness of the scarcity of natural resources that supply current methods for energy conversion, the significant increase in greenhouse gas levels in the last century [1], and the estimation of energy consumption doubling over the next fifty years [2] has accelerated research for new methods to convert the different types of energy that we find naturally to electrical energy, the energy form most sought after in everyday life. Of all the energy consumed in the US, over one-third of energy input goes to stationary electrical power generation plants. In most electrical power plants in the US, electricity is produced by a heat engine, such as a gas turbine, and the conversion efficiency is limited by the maximum achievable efficiency, which is described by the Carnot cycle. The conversion efficiency for current electrical power plants using a heat engine for energy conversion is approximately 35%. This means that approximately 21% of all the energy input in the US is lost when using conventional conversion methods to make electricity. Additionally, when coal and natural gas are burned greenhouse gases, such as nitrous oxides and carbon dioxide, are produced [3].

Renewable energy conversion technologies are needed to severe dependence on the combustion of fossil fuels for the production of electricity. Significant progress has been made in photovoltaic devices [4, 5], and other renewable energy technologies, but the current energy demand is much larger than the current renewable energy output. Additionally, current electrical energy storage (EES) systems cannot adequately store the intermittent renewable energy, to meet current energy demands [2]. Therefore, energy demands will be met with fossil fuels, until it is

possible and economically beneficial to switch to other methods of energy conversion. Until renewable energy conversion is feasible, we must use our natural resources in the most efficient and environmentally benign manner.

1.2 Fuel Cells for Stationary Power Generation

Fuel cells convert chemical energy directly to electrical energy, bypassing combustion, which increases conversion efficiency and decreases greenhouse gas emissions. The fuel cell concept has been in the literature for more than 170 years, however, only in the past 60 years has the fuel cell been heavily researched as an alternative to combustion for chemical energy conversion [6]. Fuel cell operating temperatures range from slightly above room temperature (RT) to 1000^{o}C. Cells which operate in the higher temperature ranges can reach high energy densities and are able to provide power comparable to a small, conventional power plant [7]. Proton-exchange membrane (PEM) cells and other low temperature fuel cells, do not provide as much power as comparable high temperature fuel cells, therefore low-temperature cells are studied primarily for mobile power applications. The three commonly studied fuel cells for stationary power generation are phosphoric acid fuel cells (PAFC), molten carbonate fuel cells (MCFC), and solid oxide fuel cells (SOFC). In each cell, oxidation at the anode and reduction at the cathode allows electrons to travel through an external circuit, to power a load. Ions pass through the electrolyte to complete the circuit . The heart of SOFC systems is the electrolyte. The electrolyte largely determines the operation temperature of the cell and the fuel that can be used with the cell. Because of this, each fuel cell type is categorized and named based on its electrolyte.

Phosphoric acid fuel cells (PAFCs) have a liquid phosphoric acid electrolyte, operate near 200^{o}C, and have high power densities. The high concentration phosphoric acid is supported

by a porous, Teflon-coated silicon carbide matrix and confined by capillary forces of the small pores. Hydrogen is oxidized at the anode by a carbon (graphite) supported platinum catalyst and the proton is then transported through the acid electrolyte to the cathode. Oxygen is reduced by a carbon supported platinum catalyst at the cathode and reacts with the proton to form water which is exhausted from the system [3]. The primary benefit of the PAFC is chemical, thermal, and electrochemical stability under operating conditions which allowed rapid development and field demonstrations of PAFC systems, including a 1 MW unit demonstrated by International Fuel Cells Corporation in the 1970's [8]. Drawbacks of the PAFC include the liquid electrolyte, the necessity of platinum catalyst for electrode reactions, and low conversion efficiency. The liquid electrolyte can be lost into the fuel streams and carried out of the system over time, requiring replacement of the electrolyte after long-term operation. Balance between high porosity in the electrodes for the oxidation/reduction reactions and low porosity to prevent liquid diffusion out of the cell is important. Also, the high loading of platinum catalyst, necessary for high activity for oxidation and reduction at low operating temperatures significantly increases the cost of the system, which limits commercialization [7]. PAFC efficiencies range from 40-50% but the heat released during cell operation is of low quality for cogeneration systems, making the total system efficiency lower than comparable, stationary power systems. PAFCs also have no fuel flexibility, running only on pure hydrogen.

Molten carbonate fuel cells (MCFCs), first demonstrated in the 1950's, operate at high temperatures (600^{o}C-700^{o}C) which increases the cell efficiency (50%-60%), allows for fuel flexibility (reformate, CO, H_2), and produces high quality heat for co-generation systems which further improves conversion efficiencies. The molten carbonate and salt (Li, K) mixture electrolyte in the MCFC is supported by a porous ceramic phase which confines the electrolyte

by capillary forces. Because the cell operates at high temperatures, expensive precious metal catalysts are not necessary at the electrodes. This significantly reduces the cost of the fuel cell system [7]. At the cathode, supplied CO_2 and O_2 find electrons at the TPBs of the Li-doped NiO cathode and CO_3^{2-} ions transport to the cermet anode of Ni(metal)-(Al,Cr) where hydrogen is oxidized and water and CO_2 are formed. When NiO is doped with lithium, electron holes are formed and the electronic conductivity increases from 0.03 $\Omega^{-1}cm^{-1}$ - 47 $\Omega^{-1}cm^{-1}$, making it a viable cathode material [9]. Drawbacks of the MCFC include the necessity of CO_2 at the cathode during SOFC operation and the molten electrolyte. The overall cell reaction requires a constant supply of O_2 and CO_2 at the cathode, unlike all other fuel cells which require O_2 only. While the 600^oC to 700^oC temperature range and fuel flexibility of the MCFC is ideal for a low cost, high efficiency fuel cell, the corrosive nature of the molten carbonate electrolyte and the need for CO_2 supply at the cathode have limited its development [3].

Solid oxide fuel cells provide several practical advantages to both PAFCs and MCFCs, which make them the most viable fuel cell option for stationary electrical power conversion.

1.3 Solid Oxide Fuel Cells

Among all types of fuel cells, solid oxide fuel cells (SOFCs) have the potential to offer the highest chemical to electrical energy conversion efficiency, and have the flexibility to use a wide range of fuels including hydrocarbons (fossil fuels), coal gas, biomass, and other fuels [10-16]. When combined with gas turbines, fuel cell based electrical power plants could offer energy efficiency twice that of heat engine based plants, thus dramatically decreasing the CO_2 emissions per amount of electricity produced and eliminating nitrous oxide emissions[3].

Solid oxide fuel cells are composed of all solid-state components. The solid state electrolyte eliminates electrolyte containment problems and reduces the electrolyte and electrode reaction possibilities. The high operation temperatures, required for ionic conduction through the solid electrolyte, produce quality cogeneration heat making SOFCs the most efficient fuel cell systems. Solid oxide fuel cells can reach 85% total thermal efficiency. Most importantly, SOFCs can operate on a wide range of fuels and can facilitate indirect or direct hydrocarbon reforming. This fuel flexibility allows minimally processed natural gas to be converted to electricity directly, at twice the efficiency of conventional energy conversion processes [3].

SOFCs have a dense electrolyte that blocks gas diffusion between the electrodes, is ionically conductive, and is electronically insulating. The electrolyte must be stable in reducing and oxidizing atmospheres and must be chemically and structurally compatible with the electrode materials. This requires the electrolyte to not react with the fuel, oxidant, or electrodes for the lifetime of the cell and for the thermal expansion coefficients (TEC) of the electrolyte to be compatible with the electrodes as well. Thermal expansion matching is important for maintaining structural integrity as the cell is cycled during its operation lifespan.

The cathode is the electrode on the “air” side of the cell and is responsible for reducing the oxidant. The cathode is electrocatalytically active for oxygen reduction and electronically conductive. The cathode must be porous to allow the gaseous oxidant to easily flow to the TPB and must be stable under oxidizing conditions. In order to increase cell performance, mixed ionic-electronic conductors (MIECs) are used as SOFC cathodes to extend the triple phase boundary from the electrolyte-cathode interface into the bulk of the cathode. This mixed conduction increases the number of TPB sites which are active for oxidant reduction.

The anode is the electrode on the fuel side of the cell and is responsible for fuel oxidation. The anode is electronically conductive and electrocatalytically active for the oxidation of the fuel. Porosity is necessary for gas diffusion of the fuel to the TPB where the oxidation occurs. As in the cathode, the anode also conducts ions to increase the triple phase boundary length. The anode in SOFCs is commonly a two-phase cermet, containing a metal, most commonly nickel, and an ionically conductive ceramic phase. If the ceramic phase is identical to the electrolyte material, then the TEC match and consequently the structural stability of the cell are improved. The ceramic phase also serves as a "backbone" to prevent the anode nickel from sintering during operation at high temperatures for the lifetime of the cell. Sintering of the particles reduces the surface area and porosity, which has detrimental effects on the electrocatalytic properties and porosity of the electrode.

Two SOFC architectures have been used in the literature and in commercial cells, the tubular design and the planar design. The tubular design is used to avoid high temperature sealing requirements but the tubular design leads to low power densities. The planar cell design is easier to fabricate and can be efficiently stacked for high energy density, but high temperature sealing is critical. In either design, individual cells are connected to produce fuel cell systems that deliver large amounts of power and high voltages. The material that connects the individual cells is called the interconnect and is a critical component in fuel cell system design. The interconnect material divides the cathode side of a cell from the anode of the next cell in the stack. The interconnect must have high electronic conductivity for serial connection between the cells, but no ionic conductivity, in order to separate the oxidant from the fuel. The interconnect material must have a TEC that matches that of the other fuel cell components and the interconnect must be stable under reducing and oxidizing atmospheres [17].

The ability to use our natural resources more efficiently and to reduce pollutant emissions from the conversion process has pushed SOFCs to the front of clean energy research. However, broad commercialization of SOFC technology is hindered by the high cost of current SOFC systems which makes them unreasonable in the open market. The high cost of state of the art SOFC systems is due to the high operation temperature which is necessary for high ionic conductivity and fast fuel cell reactions. In order to reduce operating temperatures, new materials possessing high ionic conductivity and low electronic conductivity in the intermediate temperature range (450^{o}C-750^{o}C) must be developed to lower fuel cell system temperatures and costs.

1.4 Motivation

The US Department of Energy, with the National Energy Technology Laboratory (NETL), has funded the Solid State Energy Conversion Alliance (SECA) over $400M from 2000 – present to develop Solid Oxide Fuel Cells (SOFCs) for the efficient and cost-effective conversion of coal gas to electrical energy. The program includes more than 7 industrial partners, US national labs, government agencies and more than 10 research universities for core technology research and development, in which Georgia Tech is included. The alliance has successfully reduced yttria-stabilized zirconia (YSZ) SOFC stack costs by 80% in the last 10 years, however, the reduction in cost can been primarily attributed to low cost manufacturing techniques and increased cell size. To compete with conventional conversion techniques, SOFC stack costs must be further reduced. A significant cost reduction could be realized if SOFC operating temperatures were reduced below 800^{o}C, to intermediate temperatures. However, state-of-the-art YSZ SOFCs cannot operate at intermediate temperatures. New SOFC materials,

which can operate at intermediate temperatures must be developed for further reduction of SOFC stack cost.

In state of the art SOFCs, YSZ is used as the electrolyte material due to its high ionic conductivity in the temperature range 800^{o}C-1000^{o}C. Its chemical stability, mechanical strength, and ease of fabrication also make it an ideal electrolyte material. However, the conductivity of YSZ decreases significantly as the temperature decreases due to increased resistance to ion transport, making it unsuitable for intermediate temperature SOFCs (IT-SOFCs). New electrolyte materials based on solid solutions of doped barium cerate and barium zirconate, such as $BaZr_{0.1}Ce_{0.7}Y_{0.2}O_{3-\delta}$[18], have attracted wide attention due to high ionic conductivity at intermediate temperatures (450^{o}C – 750^{o}C). Doped barium cerate and barium zirconate are proton conducting oxides that have high conductivity at intermediate temperatures due to low activation energy for protonic defect transport (approximately 0.4-0.6eV [19]) when compared to oxygen vacancy transport (approximately 1.1 eV [20]) [21, 22]. In the past 30 years $BaCeO_3$-based proton conducting electrolytes have been studied extensively for use in IT-SOFCs [18, 23-26]. Yttria stabilized zirconia has been studied since the beginning of the 20th century [27] and its application in SOFCs has been rigorously optimized over the past 60 years. Because of the relative youth of proton conducting SOFCs, continued research needs to be conducted to understand the fundamental properties of intermediate temperature proton conducting oxides and to optimize their application in SOFC systems. A paradigm shift to proton conducting SOFCs could lower the operating temperature of SOFCs making them economically competitive with conventional conversion technologies.

A new material, $BaZr_{0.1}Ce_{0.7}Y_{0.1}Yb_{0.1}O_{3-\delta}$ (BZCYYb), has been discovered and presented in the literature for use in intermediate temperature SOFCs (IT-SOFCs). The BZCYYb material

displayed higher conductivity in 3%H_2O/O_2 atmosphere than the conventional electrolyte materials such as YSZ and doped ceria (GDC) below 750^oC, in the range of intermediate temperature SOFCs (IT-SOFCs), due to presumed high proton conductivity. Also, a Ni-$BaZr_{0.1}Ce_{0.7}Y_{0.1}Yb_{0.1}O_{3-\delta}$ anode demonstrated resistance to coking and sulfur poisoning under hydrocarbon and H_2S contaminated fuels [16] which is important for the direct use of coal gas or hydrocarbon fuels in SOFCs. An understanding of the electrical transport of the BZCYYb material under hydrogen, oxygen, and water containing atmospheres is lacking in the literature. Optimization of the BZCYYb material in SOFC systems has also not been attempted. In this work, the conductivity of the BZCYYb material, fabricated by the solid state reaction method, is determined in all fuel cell relevant atmospheres, the transference numbers in each atmosphere are determined and the optimization of a BZCYYb based fuel cell leads to high performance and a rational design for use in all proton conducting SOFC anodes.

CHAPTER 2

PROTON CONDUCTING SOLID OXIDE FUEL CELLS

2.1 Solid Oxide Fuel Cell Thermodynamics

2.1.1 Nernst Potential

The Gibbs free energy of a chemical reaction, including the oxidation/reduction reactions at a reversible fuel cell's electrodes, is expressed in terms of the reaction entropy and reaction enthalpy in equation 1. This energy is the maximum energy available to do useful work.

$$\Delta^r G(T,p) = \Delta^r H(T) - T \cdot \Delta^r S(T,p) \quad (1)$$

The reversible efficiency of a fuel cell is given by equation 2.

$$n_{thermo} = \frac{\Delta^r G}{\Delta^r H} \quad (2)$$

In equation 1 the temperature dependent component of $\Delta^r G(T,p)$ can be separated from the component that depends on the partial pressures of the reaction products and reactants (when the specific heat dependence on pressure is assumed to be small) (equation 3).

$$\Delta^r G(T,p) = \Delta^r G(T) - T \cdot R \cdot ln \frac{\prod a_p^{v_p}}{\prod a_r^{v_r}} \quad (3)$$

Using gas phase thermochemistry data sets, one can calculate the $\Delta^r G(T)$ term for fuel cell reactions with various fuels for a range of temperatures and determine $\Delta^r G(T,p)$ at those temperatures and at a range of partial pressures of reactants and products.

In a reversible system, the electrical work done by the system is equal to the chemical energy available to do useful work. The cell reaction emf, E_N , multiplied by the charge of the electrons gives the electrical work, as seen in equation 4.

$$\Delta^r G(T,p) = -n^{el} F E_N \tag{4}$$

Equations 3 and 4 are combined to determine equation 5,

$$E_N = \frac{-\Delta^r G(T)}{n^{el} \cdot F} - \frac{R \cdot T \cdot ln \frac{\prod P_p^{v_p}}{\prod P_r^{v_r}}}{n^{el} \cdot F} \tag{5}$$

then, after simplification, we come to the Nernst Equation (equation 6) [6, 28].

$$E_N = E^o - \frac{RT}{nF} ln \frac{\prod P_p^{v_p}}{\prod P_r^{v_r}} \tag{6}$$

The potential measured at equilibrium, with no load, is the open circuit voltage (OCV) of the cell and is equal to the Nernst Potential when there is no electronic leakage across the electrolyte or significant interfacial polarization resistance [29]. When the circuit is closed, the cell voltage drops due to activation polarization and concentration polarization at the electrodes and ohmic polarization in the electrolyte, leading to equation 7.

$$E_N = E^o - \frac{RT}{nF} ln \frac{\prod P_p^{v_p}}{\prod P_r^{v_r}} - |\eta_{cathode}| - |\eta_{anode}| - |\eta_{electrolyte}| \tag{7}$$

2.1.2 Oxygen Anion and Proton Conducting SOFCs

Figure 1 distinguishes the proton conducting SOFC from the oxygen anion conducting SOFC. The ionic charge carrier and the location of water formation are the important differences.

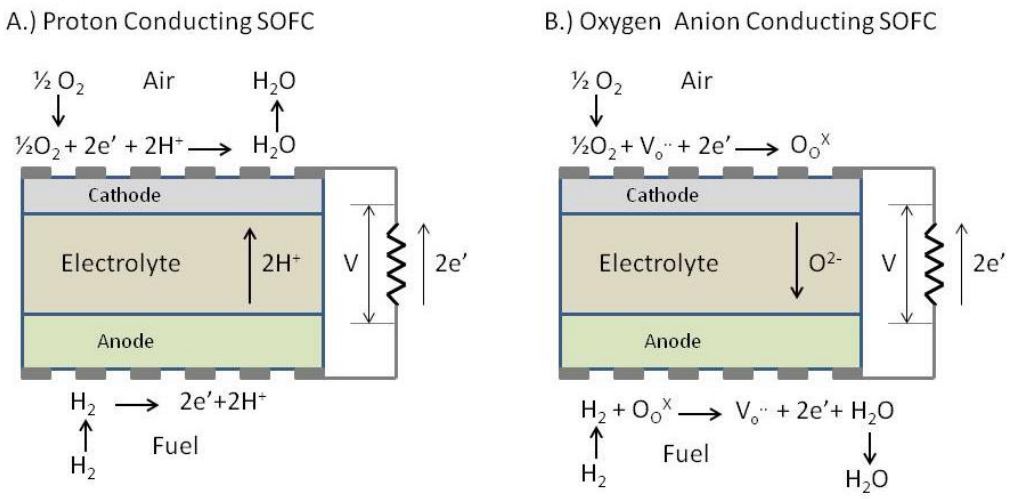

Figure 1: Schematic of the A.) Proton Conducting SOFC and B.) Oxygen Anion Conducting SOFC

Equations 8 and 9 are the electrochemical half-reactions that occur at the anode and cathode, respectively, for an oxygen anion conducting SOFC. Notice that water is produced at the anode or "fuel side" electrode.

Anode: $$H_2 + O_O^X = H_2O + V_{\ddot{O}} + 2e^{'} \quad (8)$$

Cathode: $$\frac{1}{2}O_2 + V_{\ddot{O}} + 2e' = O_O^x \quad (9)$$

The overall reaction for a hydrogen/air SOFC is the production of water and is described by equation 10, regardless of the path of the charge carrier.

$$H_2 + \frac{1}{2}O_2 = H_2O \quad (10)$$

Water produced at the anode in an oxygen anion conducting SOFC mixes with the fuel, lowering the cell voltage and efficiency. We know from equation 6 that the partial pressure of the gases at the electrodes affects the local Nernst voltage. When hydrogen is used as fuel, the fuel utilization rate is given by equation 11.

$$U_{fH_2} = 1 - \frac{y_{H_2,O}}{y_{H_2,I}} \quad (11)$$

Where $y_{H_2,I}$ is the molar concentration of the total molar flow at the anode inlet, I, and $y_{H_2,O}$ is the molar concentration of the total molar flow at the outlet, O. Also, we know that for every molecule of H_2 utilized, one molecule of water is formed, (12).

$$\dot{n}_{H_2,Utilized} = \dot{n}_{H_2O,O} \quad (12)$$

So the total fuel utilized, U_{fH_2}, is equal to the percentage of the outlet molar flow that is water, or the molar concentration, $y_{H_2O,O}$. As the fuel utilization increases, the molar concentration of water in the anode increases. Combing equations 6 and 10 (Nernst potential and water reaction) we can see that as the partial pressure of water in the fuel stream increases, the Nernst potential decreases, therefore, as the utilization of the fuel increases, the Nernst potential decreases.

For a proton conducting SOFC, the anodic and cathodic reactions can be described by reactions 13 and 14 respectively.

Anode: $$H_2 = 2H^{\cdot} + 2e^{-} \quad (13)$$

Cathode: $$\frac{1}{2}O_2 + 2H^{\cdot} + 2e' = H_2O \quad (14)$$

The SOFC with a proton conducting electrolyte produces water at the cathode, leaving the fuel pure. Therefore the Nernst potential is not dependent on the fuel utilization at the anode side, and the SOFC based on a proton conducting electrolyte can achieve a higher potential.

For a mixed oxygen anion and proton conducting SOFC, both reactions 8 and 13 occur at the anode while reactions 9 and 14 occur at the cathode. Therefore, water is produced at both sides.

We know from equation 12 that for every molecule of hydrogen consumed, one molecule of water is formed. Also the molar flow of electrons is related to the molar flow of hydrogen molecules by equation 15,

$$\dot{n}_{el} = 2\dot{n}_{H_2,utilized} \tag{15}$$

So the current can be related to the molar flow rate of water in a mixed oxygen anion and proton conducting SOFC as seen in equation 16,

$$I = \dot{n}_{el} \cdot (-e) \cdot N_A = -\dot{n}_{el} \cdot F = -2\dot{n}_{H_2,utilized} \cdot F \tag{16}$$
$$= -2(\dot{n}_{H_2O,O(cathode)} + \dot{n}_{H_2O,O(anode)}) \cdot F$$

Therefore, the total molar flow rate of water can be calculated from the current through the cell during operation. Similarly, the molar flow rate of water produced on the anode side is related to the oxygen anion charge carriers and the water produced on the cathode side is related to the protonic charge carriers. The ionic transference numbers can be calculated from the amount of water collected at each electrode.

2.2 Barium Cerate Based Proton Conductors for Intermediate Temperature SOFCs

Though most possible perovskite oxide compositions had been fabricated and tested by 1955 by Galasso, significant ionic conductivity in the perovskite oxides was not discovered until 1961 when Stephenson and Flanagan used the concentration cell-OCV method, a technique first used by Wagner [30], to verify ionic conduction in the common perovskite material, lead zirconate titanate (PZT). While the ionic conduction in the first-studied perovskite oxides was very low, it led to the testing and discovery of many perovskites with higher ionic conductivity, such as the $SrCeO_3$-based and $BaCeO_3$-based systems. Proton conducting perovskite oxide research has attracted much attention over the past three decades by authors Iwahara, Knight,

Bonanos, Kreuer and others, due to the complexity of the materials and the potential for application in intermediate temperature SOFCs (IT-SOFCs), hydrogen separation membranes [31, 32] and hydrogen sensors [33]. Proton conduction at temperatures near the boiling point of water was common, however the discovery and understanding of proton conduction at intermediate temperatures ($450^{o}C$-$750^{o}C$) became beneficial, especially for use in electrochemical devices [34]. The research of $BaCeO_3$-based systems asks many questions about the electrical conductivity of the system and how dopants and operating atmospheres affect the conductivity. In order to understand the electrical properties of the $BaCeO_3$-based systems for application in IT-SOFCs, the literature of the past three decades and the work of Iwahara, Knight, Bonanos, Kreuer and new researchers in the field will be examined.

2.2.1 Crystal Structure of $BaCeO_3$-based systems

$BaCeO_3$-based material systems have the perovskite crystal structure (ABO_3) which can host cation charge combinations of $A^{1+}B^{5+}O_3$, $A^{2+}B^{4+}O_3$, $A^{3+}B^{3+}O_3$. The cubic perovskite structure is shown in Figure 2. For perovskite structures that exhibit high ionic conduction, the A-site hosts a 2+ cation and the B-site hosts a 4+ cation. The oxygen anions and B-site cations form a BO_6 octahedra and the divalent cation sits in the larger A-site. The structure has large free volume which is affects ionic transport and the structure can accommodate a large range of dopants, with a large range of ionic radii.

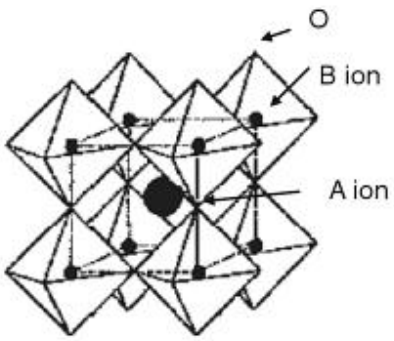

Figure 2: Ideal Perovskite Structure [34]

In common perovskite materials the cubic structure is rarely observed. For the perovskite structure to be cubic, exact length ratios of each of the bonds in the structure must be satisfied. Because these requirements are rarely satisfied, however, perovskite structures are often distorted from the cubic structure, especially at low temperatures. A tolerance factor, t, has been defined (equation 17) to describe the deviation of a perovskite structure from the ideal structure.

$$t = (r_A + r_O)/\sqrt{2}(r_B + r_O) \tag{17}$$

Perovskite oxides can conduct protons or oxygen anions and can also be electronically conductive based on the atmosphere and the temperature. In undoped perovskite oxides, the ionic conductivity is low. However, a significant increase in ionic conduction is observed when lower valent cations are doped into the material. By doping the A- or B- site of the perovskite with cations of lower valance, extrinsic charged defects are formed to maintain electroneutrality. For a M_2O_3 dopant that will sit in the B-site of the $A^{2+}B^{4+}O_3$ perovskite lattice, charge compensating oxygen vacancies will form in the lattice by the following defect equilibrium (18).

$$M_2O_3 + 2AO = 2A_A^x + 2M_B' + 5O_O^x + V_{\ddot{O}} \tag{18}$$

Oxygen anions (oxygen vacancies) migrate through the $BaCe_{1-x}M_xO_{3-\delta}$ perovskite lattice by oxygen vacancy, $V_{\ddot{O}}$, hopping. The increase in conductivity after doping of trivalent cations in the B-site can be attributed to the formation of oxygen vacancies.

2.2.2 Ionic and Electronic Conduction in $BaCeO_3$-based systems

In the 1980's Iwahara and co-workers identified proton conduction and oxygen anion conduction in the perovskite materials systems, $SrCe_{1-x}M_xO_{3-\alpha}$ and $BaCe_{1-x}M_xO_{3-\alpha}$, (M=trivalent rare earth dopant) and continued studying and publishing papers about the systems throughout the 1990's. An early paper identified the proton conduction of $SrCe_{1-x}M_xO_{3-\alpha}$ for use in steam electrolysis and hydrogen separation [35]. A concentration cell was designed and a high, stable EMF was observed when the air in each of the electrode compartments had varying humidity but constant oxygen partial pressures. Oxygen anion conduction alone could not explain the results and the authors proposed that proton conduction must be occurring in the material. To verify protonic conduction, hydrogen was supplied on one side of the membrane and argon was used as the sweeping gas on the other. After operation, hydrogen was detected on the argon side by gas chromatography, undoubtedly proving the occurrence of protonic transport in the system. These experiments were the first direct demonstration of intermediate proton conduction in materials at a sufficient level for use in electrochemical device applications, and led to the eventual development of the hydration reaction equation (19) which explains the hydrogen transport as a result of a gradient in P_{H_2O} in the H_2O/O_2 concentration cell.

$$H_2O + O_O^X + V_{\ddot{O}} \leftrightarrow 2OH^{\cdot} \qquad (19)$$

Protons are incorporated into the lattice by way of the oxygen vacancies created after trivalent doping of the B-site. Dopants substituted into the B-site of the $SrCeO_3$ system during

the early experiments included Yb, Sc, Mg, Y, In, Zn, Nd, Sm and Dy. Results were similar but some dopants lead to led to changes in the material such as higher conductivity. By comparing the pure $SrCeO_3$ material to the doped material, a significant increase in conductivity was observed [35].

Another defect reaction was discovered for the trivalent doped cerates in environments with high P_{O_2} and low P_{H_2O}. In these conditions, electronic defects form in the material, via oxygen vacancies, according to the defect reaction (20) [24, 36].

$$V_{\ddot{O}} + \frac{1}{2}O_2 \leftrightarrow O_O^X + 2h^{\cdot} \quad (20)$$

This condition is particularly important for the cathode side of the oxygen anion conducting SOFC and was studied. However, if sufficient H_2O is present, the oxygen vacancies will be filled by the protonic defects, significantly reducing the formation of electronic defects.

Next the researchers worked to determine when the doped material would conduct by oxygen vacancies and when by protons or if mixed ionic conduction could occur. In 1984, two groups published work on the $BaCe_{1-x}M_xO_{3-\alpha}$ system [37]. One group studied $BaCe_{1-x}Yb_xO_{3-\alpha}$ and found protonic conduction in the oxide. Similarly, another group [38] doped the $BaCeO_3$ system with M_2O_3 (where M=Nd, La, Ho) oxides but surprisingly reported oxygen anion transport and p-type conduction in the system. Iwahara and coworkers tested the results of these two papers by testing the $BaCe_{1-x}M_xO_{3-\alpha}$ system (M=Nd, Ca, La, Y) by the concentration cell - OCV method to verify the mobile charge carriers present and to compare conductivity measurements to the conductivities measured from the $SrCe_{1-x}M_xO_{3-\alpha}$ system. The tests confirmed the presence of p-type conduction in the material and the protonic conduction at intermediate temperatures and in water containing atmospheres but did not uncover the oxygen

anion conduction. More significantly however, the conductivity measured in the $BaCe_{1-x}M_xO_{3-\alpha}$ systems was higher for all dopants tested (except Ca) and that the $BaCe_{1-x}M_xO_{3-\alpha}$ system's conductivity at 1000^oC in wet air was three times higher than the conductivity previously reported for the $SrCe_{0.95}Yb_{0.05}O_{3-\alpha}$ system. The high conductivity discovered in the $BaCeO_3$-based material system propelled $BaCeO_3$-based systems to the front of proton conducting oxide research for many years. At the end of the article, the author suggests that though not discovered in these test conditions, oxide ion conductivity could be present in the $BaCe_{1-x}M_xO_{3-\alpha}$ system under fuel cell conditions and that the conduction mechanisms could be more complicated than in the SrCeO3-based materials system [37]. From subsequent studies, both proton and oxygen anion charge carriers as well as electronic charge carriers were confirmed in the $BaCeO_3$-based materials depending on the testing atmosphere. The mixed reports from the two papers mentioned above demonstrate the complexity of the electrical conductivity in the BaCeO3-based systems and show how easily incomplete conclusions can be drawn from experimental data. Special care should be taken to ensure the real properties of the material under all relevant conditions are understood and reported.

2.2.3 Proton to Oxygen Anion Charge Carrier Transition

Continued work by Bonanos [39, 40], Iwahara [24], and Taniguchi [41], in the early 1990's, further confirmed mixed oxygen anion, protonic, and electronic conductivity in the $BaCeO_3$-based systems. Interestingly, the workers distinguished an ionic conduction transition in the $BaCe_{1-x}M_xO_{3-\delta}$ (M=Gd, Sm) material systems from majority proton charge carrier to majority oxygen anion charge carrier with increasing temperature. By measuring the water evolution at each of the electrodes during hydrogen-oxygen fuel cell tests, majority protonic conduction was confirmed at temperatures near 600^oC and majority oxygen anion conduction near 1000^oC under

fuel cell conditions. It is apparent that proton conduction has lower activation energy than oxide ion conduction because of the higher temperature necessary for oxide ion transport in the system. However, it was not apparent what other parameters effect the type of ionic conduction present in a material at a given temperature.

In 1994, Iwahara and coworkers determined the transference numbers of the $BaCeO_3$-based systems as a function of dopant ionic radius under fuel cell conditions by measuring the water evolution at each electrode, using a hygrometer. The work confirmed the transition from protonic conduction to oxygen anion conduction with increasing temperature. The work also identified a significant change in transport number when the trivalent dopant in the $BaCe_{.9}M_{.1}O_{3-\alpha}$ system (M=Yb, Y, Dy, Gd, Sm, Nd) was changed. This work began to link the properties of the $BaCeO_3$-based materials to the dopant size. Figure 3 is the result of this work which tested and plotted the oxygen anion and protonic transference numbers against the dopant ionic radius to understand the relationship.

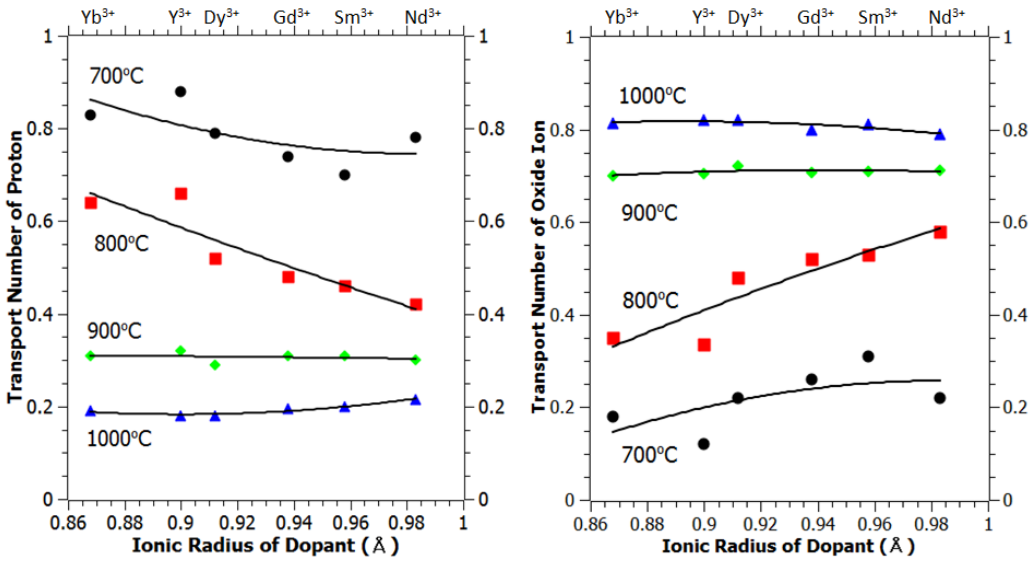

Figure 3: Ionic Transport Number vs. Ionic Radius of Dopant for $BaCe_{0.9}M_{0.1}O_{3-\alpha}$ (reproduced)[23]

Dopants with larger ionic radii increase the oxygen anion transport number significantly at lower temperatures (which automatically lowers the proton transference number), revealing a correlation between transference number, dopant, and structure [23].

The transference numbers in the $BaCeO_3$-based systems are important to understand when applying the materials in SOFC systems. When the charge carrier changes from majority protonic carriers to majority oxygen anion carriers, the fuel cell reaction products are formed at different sides of the cell. Oxygen anion conduction generates reaction products at the anode and protonic conduction generates fuel cell reaction products at the cathode. This not only effects the voltage of the cell [6] but it also effects the ability of the cell to directly reform hydrocarbons. Some oxygen anion conduction is necessary for direct oxidation of the hydrocarbons on the anode side of the SOFC and to prevent carbon coking, however, when the water is produced on the cathode side of the SOFC the cell efficiency is improved. Carefully selected B-sites dopants for the $BaCeO_3$-based systems could tailor the material to provide partial oxygen anion conduction for hydrocarbon reforming, balanced by protonic conduction to increase voltage and efficiency of the cell.

2.2.4 Crystal Symmetry Effect on Ionic Transport

In the literature, the effect of dopant size on defect transport has been extensively studied. In earlier papers, such as published by Iwahara [23], a strong correlation between defect transport and crystal symmetry was reported. This was supported by the fact that larger dopants increase the free volume in the perovskite structure increasing the critical transport radius, allowing more room for large oxygen vacancies to move from one lattice position to another. However, as dopant ionic radius increases, distortion in the lattice occurs. Distortion in the lattice

decreases oxygen vacancy mobility due to energetically unequal lattice oxygen sites which may trap oxygen vacancies [25]. Both the tolerance factor (which quantifies the symmetry) and free volume are plotted against dopant radius in Figure 4. The optimal dopant will be found at the intersection of highest unit cell free volume and highest crystal symmetry. Figure 5 is a plot of the conductivity of trivalent rare-earth doped $BaCe_{0.9}M_{0.1}O_{3-\delta}$ (M=Yb, Y, Gd, Sm, Nd, La) as a function of dopant ionic radius at 300^{o}C, 500^{o}C, and 600^{o}C [42]. The material systems with highest conductivity match the dopant distance from the crossover point of highest free volume and highest crystal symmetry. However, it should be noted that reports in the literature are not in agreement with which doped $BaCeO_3$-based system has the highest conductivity. The reported conductivity depends on fabrication technique, testing conditions and testing technique.

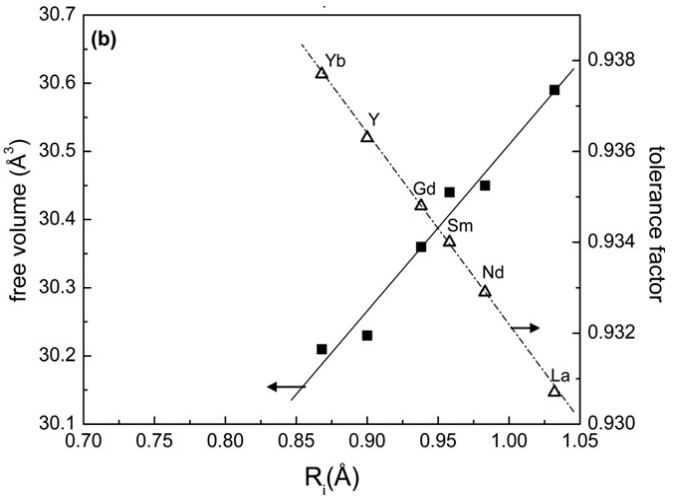

Figure 4: Variation of the free volume (V_f) and the tolerance factor (t) in $BaCe_{0.9}Ln_{0.1}O_{3-\delta}$ (Ln = La, Nd, Sm, Gd, Tb, Yb and Y) compounds as a function of the ionic radius. [42]

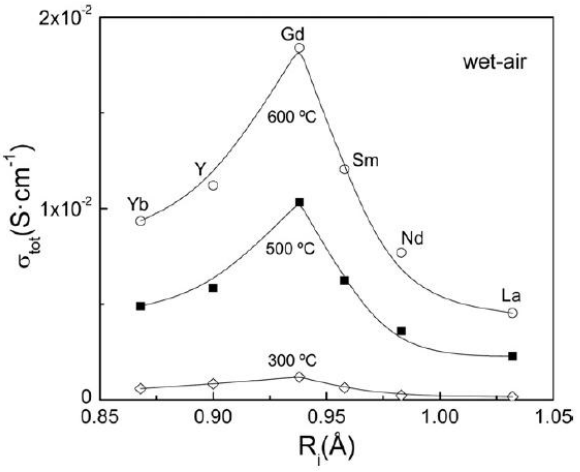

Figure 5: Variation of the total conductivity at 300, 500, and 600°C in $BaCe_{0.9}Ln_{0.1}O_{3-\delta}$ compounds as a function of the rare-earth radius of the dopant in wet air atmosphere [42]

The effect of crystal symmetry and free volume on conductivity can also be observed by comparing the $BaCeO_3$- and $SrCeO_3$-based systems. Experimentally, $BaCeO_3$- based materials have higher ionic conductivity than $SrCeO_3$-based material systems. Though similar materials, the $BaCeO_3$-based system is close to the ideal cubic perovskite at high temperatures and has high free volume [25]. However, the $SrCeO_3$-based system has orthorhombic symmetry even at high temperatures and has lower free volume than the $BaCeO_3$-based systems. The low symmetry and low free volume of the $SrCeO_3$-based systems creates oxygen sites with different energies. This decreases the mobility of defects and decreases the conductivity [43]. Experimental results must be examined to determine the optimal dopant for the system.

2.2.5 Optimum Dopant Concentration

Trivalent, rare earth dopants are used as dopants in the $BaCeO_3$ system to generate oxygen vacancies (equation 18) and make protonic defect formation possible. The trivalent rare earth ions have an ionic radius, similar to Ce^{4+}, and preferentially sit in the B-site. However, trivalent dopants can incorporate onto the Ba^{2+} site, especially when there is a deficiency in the

Ba^{2+} site. Cation nonstoichiometry can be caused by evaporation of BaO during material fabrication and processing. Incorporation of trivalent dopants at the Ba^{2+} site will decrease the concentration of oxygen vacancies, $V_{\ddot{O}}$, lowering the electrical conductivity of the system [44].

To increase the concentration of oxygen vacancies in the system and also the concentration of protonic defects in the system, the trivalent dopant fraction should be increased. However, previous studies of trivalent, rare-earth dopants on the B-site reveal that the highest electrical conductivity is achieved when the dopant level is limited to 15% - 20% in the $BaCe_{1-x}M_xO_{3-\delta}$ system when M= Gd [45], Nd, Yb [46], Y [47], and Sm [48]. XRD patterns and XAFS spectra of $BaCe_{1-x}Y_xO_{3-\delta}$ samples with x=0.02, 0.1, 0.2, 0.3, prepared by the sol-gel method, were analyzed [47] to determine the solubility limit of yttrium oxide in the barium cerate matrix. XRD patterns show no indication of inhomogeneity in the material, however, XAFS reveals the presence of Y_2O_3 phase at $x \geq 0.2$, likely segregated to the phase boundaries [47]. Another study [49] of the same material system reports Y_2O_3 and BaY_2O_4 phase formation in samples with $x \geq 0.2$ after solid state reaction powder preparation. These phases do not participate in ionic conduction and limit the mobility of defects in the system. Also, at higher doping levels, defect clustering could occur, which would also decrease the conductivity of the system.

2.2.6 $BaCeO_3$ - $BaZrO_3$ Solid Solution

SOFCs fueled by hydrocarbon fuels must be chemically stable to CO_2 containing environments. $BaZrO_3$ is a perovskite system with higher stability under CO_2 conditions than $BaCeO_3$ systems due to the higher electronegativity of zirconium than cerium and higher covalency of the Zr/O bond [43]. A solid solution of doped $BaCeO_3$ and doped $BaZrO_3$ has been studied for use as an SOFC electrolyte material. While the $BaZrO_3$ system has benefits for

chemical stability, the reported electrical conductivity of $BaZrO_3$-based sintered pellets is lower than $BaCeO_3$. This is due to the high grain boundary impedance in sintered $BaZrO_3$-based pellets. A recent work [50] used pulsed laser deposition (PLD) to created $BaZr_{0.8}Y_{0.2}O_{3-\delta}$ (BZY) single crystal thin films. Researchers found that the electrical conductivity increased by two orders of magnitude in the sample. The high conductivity is attributed to the high bulk conductivity of BZY with no grain boundaries to decrease the conductivity. However, when processed using conventional, cost-effective ceramic fuel cell processing techniques, the low sinterability of $BaZrO_3$ creates small grains and large brain boundary areas. Therefore, in order to be considered as an electrolyte material for SOFCs, a solid solution of $BaCeO_3$ and $BaZrO_3$ with improved sinterability and conductivity has been studied.

XRD of the $BaCe_{0.9-x}Zr_xY_{0.1}O_{3-\delta}$ ($0.0 \leq x \leq 0.9$) material revealed no secondary phases and a steady decrease in the lattice parameter with increasing zirconium content followed expectations. After exposing the systems to 100% CO_2, XRD revealed that the sample with 10% zirconium content oxide degraded while the solution with 40% zirconium showed no degradation. The conductivity, as predicted, decreased as zirconium content increased due to decreased sinterability and small grain size [51]. More recently, in 2006, a report identifies $BaZr_{0.1}Ce_{0.7}Y_{0.2}O_{3-\delta}$ (BZCY) to be chemically stable at 500^oC in both CO_2 and H_2O environments. XRD data of BZCY samples tested in 2% CO_2 (a more realistic value for SOFC conditions) and 15% H_2O for 7 days showed no degradation. However, samples of similar composition, but without zirconium, showed decomposition to $BaCeO_3$, CeO_2, and Y_2O_3 after seven days of exposure to 2% CO_2. It should be noted that the process used to fabricate the $BaCeO_3$-$BaZrO_3$ solid solution based materials influences the material's stability in CO_2 environments. BZCY powders, prepared by the sol-gel preparation method and the solid state

reaction method were treated to 3% CO_2 at 600^oC for seven days and the structure was examined. Powders prepared by the SSR method and calcined at higher temperatures showed no formation of $BaCeO_3$, while the powders prepared by the sol-gel method showed $BaCO_3$ formation[52]. This illustrates the sensitivity of the $BaCeO_3$-$BaZrO_3$ based material systems to fabrication techniques. However, with proper fabrication, the $BaCeZrO_3$-based materials show resistance to CO_2 under fuel cell conditions. In addition to high stability, the $BaZr_{0.1}Ce_{0.7}Y_{0.2}O_{3-\delta}$ composition also showed a high conductivity of $9x10^{-3}$ S/cm at 500^oC [22]. In general, the $BaCeO_3$ and $BaZrO_3$ solid solution is a good technique for creating high temperature proton conducting electrolytes with high chemical stability and high conductivity for use in intermediate temperature SOFCs.

2.2.7 Y^{3+} and Yb^{3+} Co-Dopants at the B-site in $BaCeO_3$-based material systems

In the literature, many rare-earth, trivalent dopants have been introduced into the B-site of the $BaCeO_3$-based material systems, including Gd [39, 45], Nd[38], Yb [46], Y [47, 53], Sm [48] to increase ionic conductivity by the creation of oxygen vacancies. In order to replace traditional oxygen anion conductors currently used in high temperature SOFCs (YSZ and doped ceria), the doped $BaCeO_3$-based systems must have higher conductivities at intermediate temperatures than the conventional materials. The protonic conduction of the $BaCeO_3$-based materials lowers the activation energy which decreases the slope of conductivity vs. decreasing temperature plot. However, because the conductivity is not high enough in some doped $BaCeO_3$-based systems, the YSZ or doped ceria could still have higher conductivity even at intermediate temperatures (450^oC-750^oC). When a mixture $BaCeO_3$-$BaZrO_3$ is used as the base material for trivalent doping (as in our experiments), the optimum dopant must be a compromise of the best dopants of the two systems. In the $BaZrO_3$ system, Y^{3+}, has been found to be the optimal dopant

for the system. The hydration of the Y^{3+} doped $BaZrO_3$ system is complete for dopant levels up to 20% (i.e. protonic defects fill all vacancies created by Y^{3+} doping). The conductivities of the $BaZr_{0.8}Y_{0.2}O_{3-\delta}$ and the $BaCe_{0.9}Y_{0.1}O_{3-\delta}$ systems are both higher than YSZ below 800^{o}C [43] . Therefore, although Y^{3+} is not the optimal dopant for $BaCeO_3$, it may be the best for the $BaCeO_3$-$BaZrO_3$ mixture. In some tests, Yb^{3+} doped into the B-site of $BaCeO_3$ showed high bulk conductivity in wet atmospheres [46], higher than Gd^{3+} or Nd^{3+} dopants. The effect of co-doping the B-site is not fully understood, but experimental work has shown that conductivities of co-doped $BaCeO_3$-based materials are higher than the conductivities of either of the materials with the individual dopants [16, 54]. The co-doping of Y^{3+} and Yb^{3+} in the B-site of $BaCeO_3$ leads to high ionic conductivity which is necessary for high SOFC performance. The conductivity of BZCYYb in 3%H_2O/O_2 is significantly higher than either YSZ or doped ceria (GDC) in the IT-SOFC region (450^{o}C – 750^{o}C) making it the best candidate for future study as the electrolyte material for IT-SOFCs. A comparison of the total ionic conductivity of BZCYYb in 3%H_2O/O_2 environment to other ionic conductors (BZCY, GDC, YSZ) used in SOFCs is shown in Figure 6.

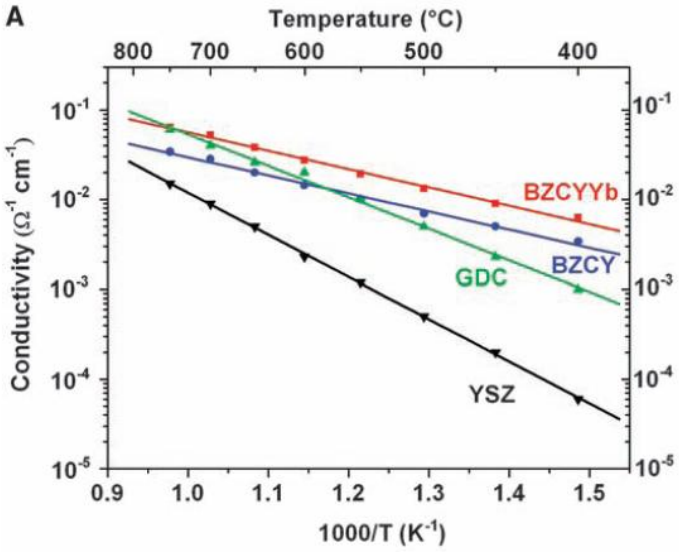

Figure 6: Comparison of total ionic conductivity in the intermediate temperature range with 3%H_2O/O_2 atmosphere for SOFC electrolyte materials [16]

In addition to high conductivity, the BZCYYb material system has shown unique tolerances to carbon coking and H_2S poisoning when used in a nickel cermet SOFC anode. The Ni-BZCYYb anode is a good catalyst for conversion of H_2S to SO_2 and can reform hydrocarbon fuel in-situ to prevented carbon deposition on the anode[16]. Further work has shown that BaO nanoislands, which easily adsorb water, form on the anode surface and prevent carbon coking [15].

Because of the high conductivity of the BZCYYb material at IT-SOFC temperatures and its tolerance to H_2S and hydrocarbon fuels when used in the anode of the SOFC, further characterization of the system should be done.

2.3 Discussion

The $BaCeO_3$-$BaZrO_3$ solid solution is a good base material system for use as an electrolyte in intermediate temperature SOFCs due to its chemical stability under SOFC conditions. By doping the B-site of the system with trivalent cations, the concentration of defects, necessary for ionic conduction, increases dramatically. The doped $BaCeO_3$-based materials exhibit oxygen anion, protonic, and electronic conduction depending on the testing atmosphere and temperature. The dopant affects the symmetry and free volume of the material, which affects the conductivity. A transition from proton conduction to oxygen anion conduction upon an increase in temperature has been verified in the system, and the transference number at each temperature depends on the size of the B-site dopant. The high conductivity of the $BaZr_{0.1}Ce_{0.7}Y_{0.1}Yb_{0.1}O_{3-\delta}$ system and the ability of the Ni-BZCYYb anode to resist coking and sulfur poisoning make it an ideal material system for continued study for use in IT-SOFC systems.

CHAPTER 3

FABRICATION OF $BaZr_{0.1}Ce_{0.7}Y_{0.1}Yb_{0.1}O_{3-\delta}$

3.1 Powder Fabrication by Solid State Reaction

Fabrication of complex oxides by the solid state reaction (SSR) method requires great care to achieve a high quality material that can be processed for use in IT-SOFC components. The purity and particle size of the commercial precursor powders affect the quality of the fabricated and processed oxide. Minor impurities (<0.25%) can greatly affect the sintering behavior and fundamental materials properties of the fabricated powders. The fabrication technique affects the uniformity of composition throughout the final material which directly affects the conductivity of the material. Also the fabrication technique effects the particle size and shape of the final powders, which effects the agglomeration tendency of the powders and the density of the sintered pellet [55]. The solid-state reaction method was used in this study to fabricate the $BaZr_{0.1}Ce_{0.7}Y_{0.2-x}Yb_x O_{3-\delta}$ material for electrical properties testing and for use in the electrolyte, anode, and cathode of the Ni-BZCYYb/BZCYYb/LSCF-BZCYYb fuel cell.

In the solid state reaction method precursor powders are calcined to create a pure, single phase material. Because the reaction between the mixed precursor powders is diffusion limited, the precursor powders are mixed and consolidated to decrease the diffusion distance and to increase the points of contact between each of the precursor powders. Accordingly, uniformity in mixing of the precursor powders promotes the solid state reaction. The kinetics of the solid state reaction determine the amount of product that is formed during the preparation timeframe. Longer reaction times and temperatures near, but not above, the melting points of the precursors and intermediates increase the rate of the reactions and facilitate the ability to produce pure,

single phase materials. Larger particles and agglomeration of precursors increases diffusion lengths, slowing the reaction rate. The solid state reaction method is a simple and economical fabrication technique. The technique, however, must be optimized to ensure complete reaction, no undesirable phases, and no contamination during the fabrication process [55].

In the literature, NiO is added in small quantities (1wt%) to BZCYYb as a sintering aid. The NiO addition lowers the necessary sintering temperature for high density pellets without significantly affecting the electrical conductivity of the material or fuel cell performance [56]. The increased sinterability is attributed to a BaY_2NiO_5 phase that forms at the interface of the similar mixture NiO and $BaZr_{0.8}Y_{0.2}O_{3-\delta}$ at 1200^{o}C. The BaY_2NiO_5 phase has a lower melting point than either NiO or $BaZr_{0.8}Y_{0.2}O_{3-\delta}$ which promotes grain growth and densification of the pellets [57]. The BaY_2NiO_5 phase was also identified in the NiO-BZCYYb mixture [56]. The NiO-BZCYYb mixture is especially important for further study because during the fabrication process of anode supported BZCYYb based proton conducting fuel cells (described in Chapter 5), diffusion of the NiO from the anode to the BZCYYb electrolyte is known to occur. Therefore, the properties of the NiO-BZCYYb mixture need to be understood in addition to the properties of the pure BZCYYb material.

In this work, pure BZCYYb powders were fabricated by the SSR method and a (1wt%)NiO-BZCYYb mixture was fabricated from the SSR BZCYYb powders. The powders were pressed into pellets, sintered, and further studied with SEM and XRD.

3.2 Experimental

3.2.1 Fabrication

3.2.1.1 BZCYYb

$BaZr_{0.1}Ce_{0.7}Y_{0.1}Yb_{0.1}O_{3-\delta}$ (BZCYYb) was prepared by the solid-state reaction method from barium carbonate (Sigma Aldrich, ≥99%, item #237108, $BaCO_3$), zirconium oxide (Alfa Aesar, 99%, stock#44886, ZrO_2), cerium(IV) oxide (Aldrich, 99.9%, item#211575, CeO_2), yttrium(III) oxide (Alfa Aesar, 99.99%, stock#11181,Y_2O_3), and ytterbium(III) oxide (Alfa Aesar, 99.9%, stock#11191,Yb_2O_3) precursor powders in stoichiometric ratio. Powders were ball-milled for 24 hours in ethanol, dried for 24 hours, crushed, and calcined at 1100^{o}C in air for 10 hours.

In order to ensure the powders were single phase perovskite, the calcination step was repeated. Between calcinations, the powders were ball milled and ground to ensure uniformity in mixing and to mitigate the formation of secondary phases. The fabrication process is represented graphically in Figure 7.

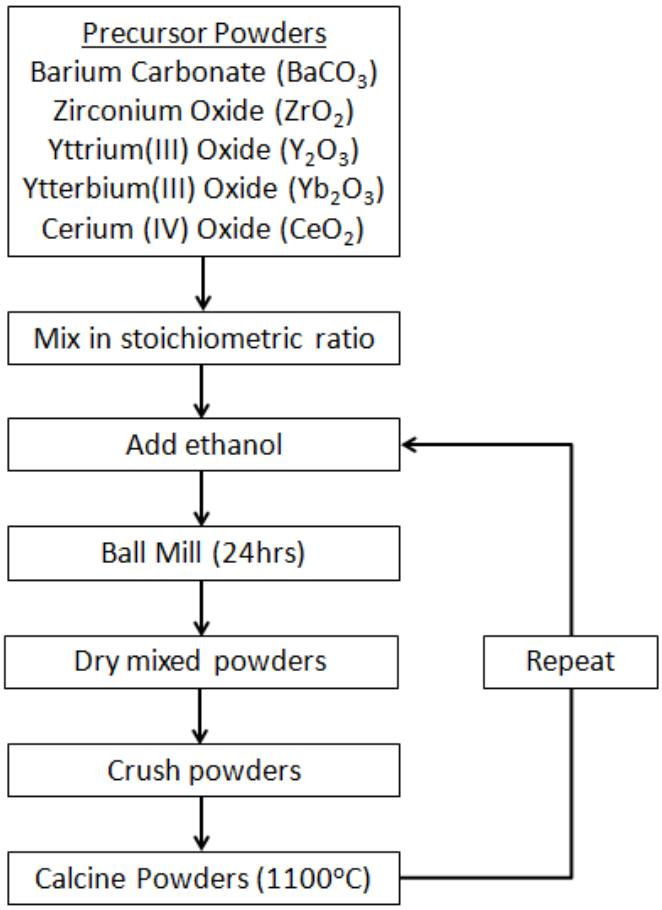

Figure 7: Solid State Reaction fabrication steps of $BaZr_{0.1}Ce_{0.7}Y_{0.1}Yb_{0.1}O_{3-\delta}$

A PANalytical X'Pert PRO powder diffractometer with Cu-Kα radiation from $2\theta=20^{o}$ to 80^{o} was used to determine the XRD pattern of the BZCYYb powder fabricated by the solid state reaction method, after the second calcination. The XRD pattern, with characteristic perovskite peaks, is shown in Figure 8.

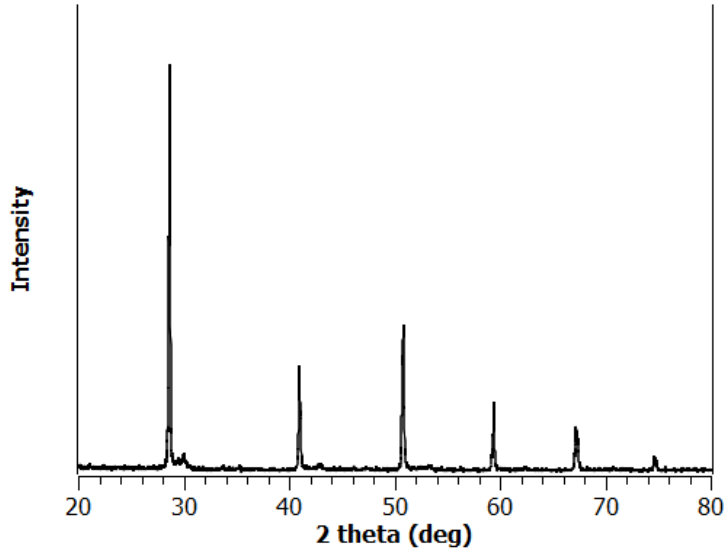

Figure 8: XRD pattern of $BaZr_{0.1}Ce_{0.7}Y_{0.1}Yb_{0.1}O_{3-\delta}$ powders powder fabricated by the solid state reaction method

The BZCYYb powders were uniaxially pressed ($18x10^3$ psi) into pellets (d≈13mm, thickness≈600μm). The pellets were then sintered at 1550^{o}C in air for 10 hours. The high sintering temperature and length of time necessary for the ceramic to densify, causes loss of BaO [58], which can significantly affect the conductivity of the sample. Special processing techniques are necessary to create a material of correct and repeatable stoichiometry [59]. In order to ensure quality samples during sintering, the BZCYYb pellets were covered with excess BZCYYb powder to decrease the evaporation of BaO as shown in Figure 9. The excess BZCYYb powder also shields the samples from the alumina crucible which studies have shown, can react with $BaCeO_3$-based materials to form $BaAl_2O_4$ and promote the formation of ytrria-doped CeO_2, which also effects the materials properties [60].

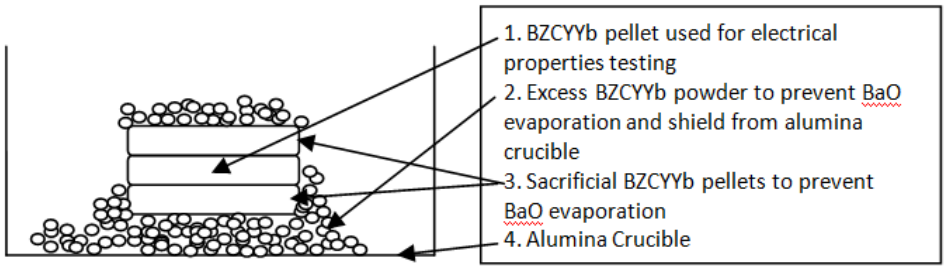

Figure 9: Diagram of $BaZr_{0.1}Ce_{0.7}Y_{0.1}Yb_{0.1}O_{3-\delta}$ pellet sintering configuration

A cross sectional SEM image and top surface SEM image of the sintered BZCYYb pellets are shown in Figure 10. The images reveal that the pellets are not completely dense after sintering, but the majority of the pores in the sintered pellets appear to be closed. Although closed porosity will influence the conductivity measurements of the pellets, closed porosity prevents gas permeation, making the sintered pellet still usable as a membrane for some electrical measurements.

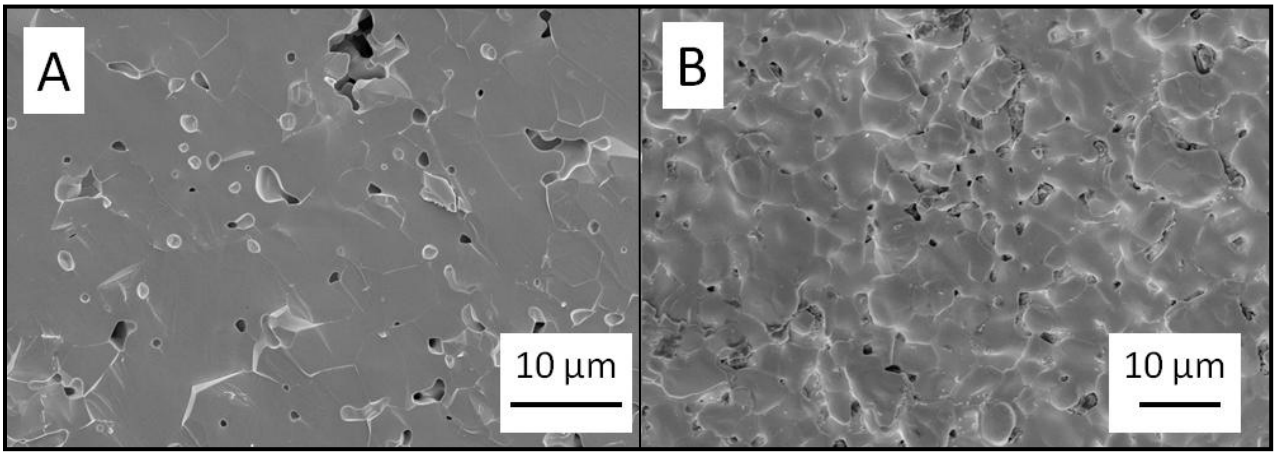

Figure 10: SEM image of sintered $BaZr_{0.1}Ce_{0.7}Y_{0.1}Yb_{0.1}O_{3-\delta}$ pellet A.) cross-section and B.) top surface

3.2.1.2 NiO-BZCYYb

Nickel oxide (Alfa Aesar, stock #45094, NiO) and the $BaZr_{0.1}Ce_{0.7}Y_{0.1}Yb_{0.1}O_{3-\delta}$ powders fabricated by the SSR method were mixed in a 1:100 weight ratio. The powders were ball-milled

in ethanol for 24 hours, dried, uniaxially pressed ($18x10^3$ psi) into pellets (d≈13mm, t≈600μm), and sintered at 1400°C for 10 hours.

The sintered NiO-BZCYYb pellets are a black color, while the sintered, pure BZCYYb pellets are light brown. An SEM image of the NiO-BZCYYb sintered pellet is shown in Figure 11. Although the sintering temperature (1400°C) was 150°C lower than the pure BZCYYb pellet sintering temperature (1550°C), the sintered NiO-BZCYYb pellet contains less porosity and appears to be sintered well.

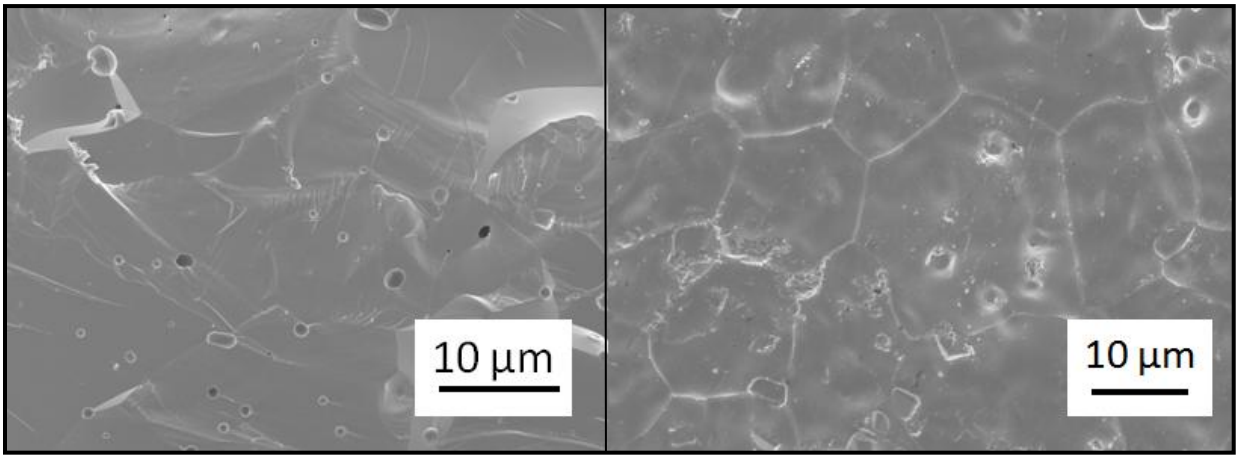

Figure 11: SEM image of sintered (1wt%)NiO-$BaZr_{0.1}Ce_{0.7}Y_{0.1}Yb_{0.1}O_{3-\delta}$ pellet A.) cross-section and B.) top surface

In other experiments, pellets were sintered from a (.25wt%)NiO-BZCYYb mixture and similar changes (black color and increased density) were observed when compared to the pure BZCYYb pellets. This shows the sensitivity of the BZCYYb material to contamination in the fabrication process. Low fractions of contaminants can lead to significant changes in the BZCYYb material.

3.2.2 XRD Characterization of Sintered BZCYYb Pellets

XRD was used to analyze the pure BZCYYb oxide pellet after sintering. At room temperature, we observed broadening and splitting of the characteristic cubic perovskite peaks in the BZCYYb material after sintering at 1550^{o}C for 10 h, as seen in Figure 12. After slight changes in sintering times, temperatures, atmospheres, and precursor powders, we continued to observe the same splitting at the cubic perovskite peak positions.

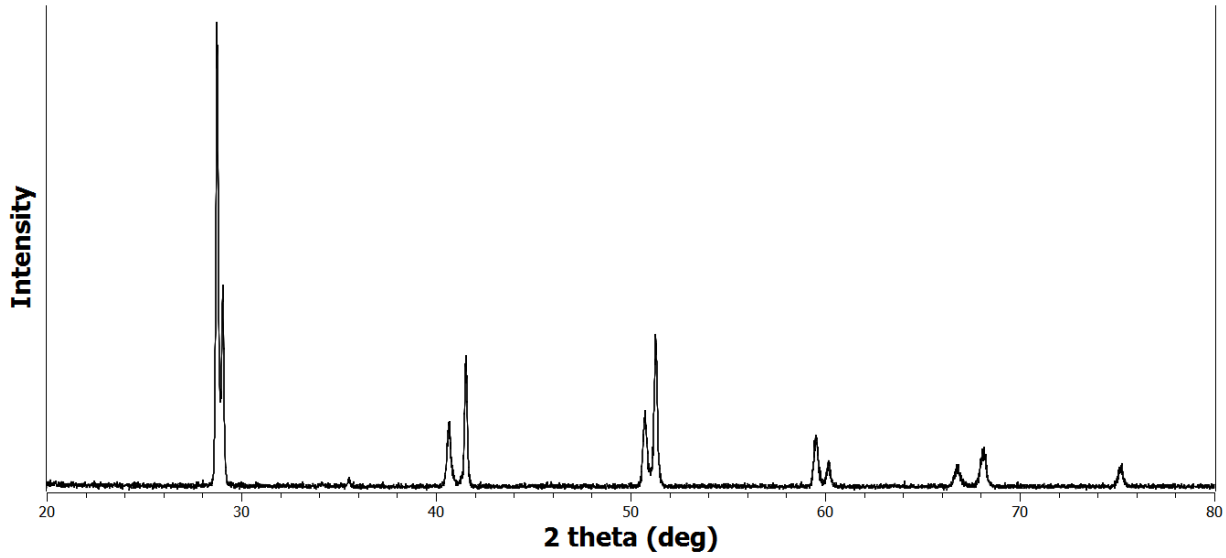

Figure 12: XRD pattern of sintered $BaZr_{0.1}Ce_{0.7}Y_{0.1}Yb_{0.1}O_{3-\delta}$ pellets

The reason for the split peaks is not clearly understood. However, in order to determine the structure of the sintered BZCYYb pellets at operating temperatures (550^{o}C-750^{o}C), high-temperature XRD (HT-XRD) was performed on the sample. A PANalytical X'Pert PRO powder diffractometer with Cu-Kα radiation from 2θ=20^{o} to 80^{o} with a HTK1200 Anton-Paar oven furnace sample holder was used for analysis. XRD patterns were collected every 25^{o}C from RT to 800^{o}C. Select patterns which reveal peak trends with increasing temperature are shown in

Figure 13. It is clear that at 25°C the characteristic perovskite peaks are split and that at 800°C, the peaks are no longer split and the widths of the peaks are reduced.

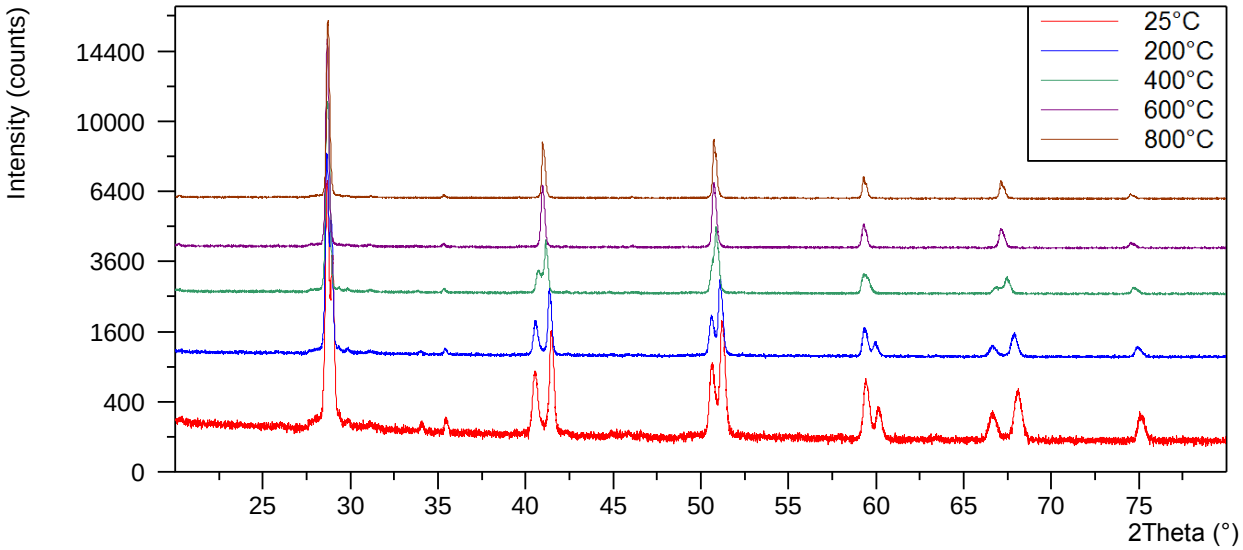

Figure 13: HT-XRD pattern of sintered $BaZr_{0.1}Ce_{0.7}Y_{0.1}Yb_{0.1}O_{3-\delta}$ pellets from 25°C – 800°C

Above 600°C the peak splitting disappears and the pattern is similar to that of BZCYYb powder after calcinations at 1100°C. The reduction of peak width with increased temperature is an indication that the BZCYYb sintered pellets have low symmetry at room temperature and higher symmetry above 600°C similar to the other $BaCeO_3$-based systems reported in the literature.

3.2.3 XRD Characterization of Sintered NiO-BZCYYb Pellets and BZCYYb electrolyte

HT-XRD was performed on the NiO-BZCYYb sintered pellets in the same manner as in the BZCYYb HT-XRD analysis and the results are shown in Figure 14. The XRD pattern of the NiO-BZCYYb pellets at room temperature reveals the characteristic, narrow perovskite peaks without peak splitting. The peak width decreases slightly as the temperature increases to 800°C.

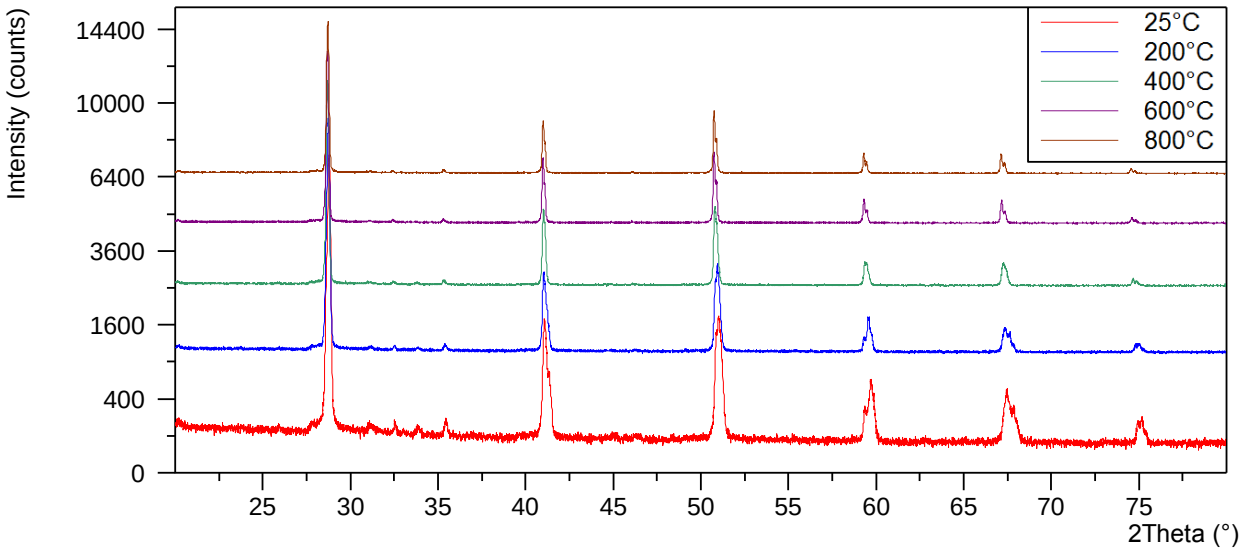

Figure 14: HT-XRD pattern of sintered (1wt%)NiO-$BaZr_{0.1}Ce_{0.7}Y_{0.1}Yb_{0.1}O_{3-\delta}$ pellets from 25^{o}C – 800^{o}C

Figure 15 is the XRD pattern from the BZCYYb electrolyte, sintered at 1400^{o}C on a NiO anode substrate. As mentioned above, NiO diffuses into the electrolyte during SOFC electrolyte fabrication. The NiO diffusion into the electrolyte can be verified by the black color of the BZCYYb electrolyte prepared on the NiO anode support. The room temperature XRD pattern has sharp peaks and no peak splitting is observable.

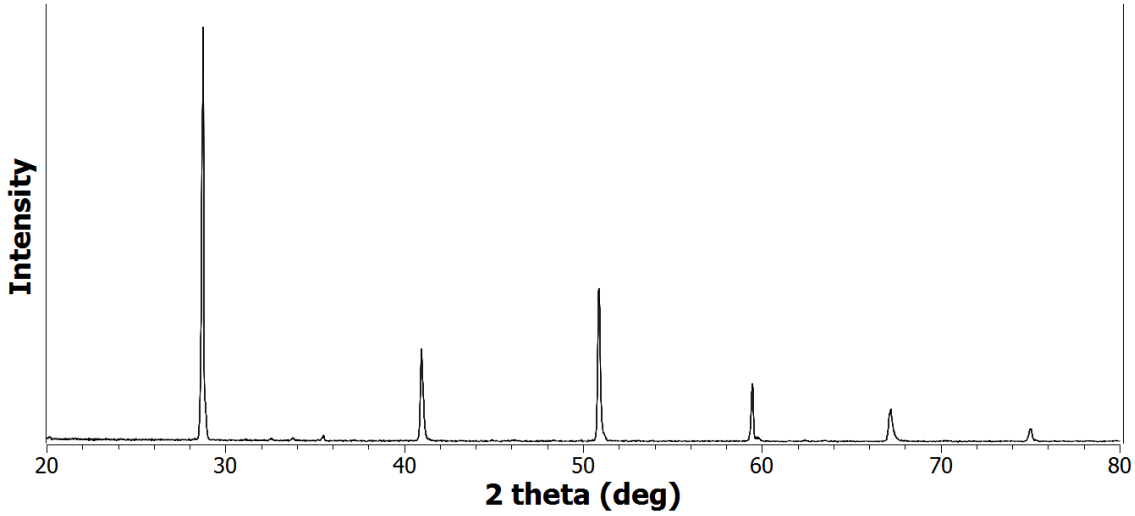

Figure 15: XRD pattern of $BaZr_{0.1}Ce_{0.7}Y_{0.1}Yb_{0.1}O_{3-\delta}$ electrolyte on NiO anode support

3.3 Discussion

Peak splitting occurs in the pure BZCYYb pellets, sintered at 1550^{o}C for 10 hours. However, HT-XRD reveals that the peak splitting disappears at temperatures above 600^{o}C. When a small amount of NiO is added to the BZCYYb material, a change in color, sintering behavior, and crystal structure occurs. The NiO addition is beneficial for achieving high density pellets at 1400^{o}C, 150^{o}C less than the sintering temperature of pure BZCYYb. In the NiO-BZCYYb sintered pellets and in the BZCYYb electrolytes fabricated on the Ni-BZCYYb anodes, XRD patterns did not reveal peak splitting of the characteristic perovskite peaks. Laboratory scale XRD alone was used to determine the patterns of the BZCYYb material in this work. Therefore, no attempt to refine the exact structure at specific temperatures was made. However, synchrotron XRD and neutron diffraction data of similar $BaCeO_3$-based systems from the literature will be used to help explain the peak splitting.

XRD and neutron diffraction studies in the literature [25, 61-63] indicate that the peak splitting in XRD patterns with temperature can be attributed to the structural phase changes that occur in the $BaCeO_3$-based systems.

Studies indicate that the $BaCeO_3$ system undergoes 3 phase transitions from 4.2K to 1273K [64]. The cubic structure is present at high temperatures but subsequently transforms to lower symmetry rhombohedral, orthorhombic, and monoclinic structures as the temperature decreases. The structural phase transformations are attributed to changes in the A-O and B-O bond lengths of the perovskite structure due to thermal expansion. The Goldschmidt tolerance factor decreases from the ideal t=1 as the temperature decreases, causing the BO_6 octahedra to tilt to accommodate [65]. The rotation of the BO6 octahedra causes the XRD pattern to change.

In the $BaCe_{0.8}Y_{0.2}O_{2.9}$ system, neutron diffraction data revealed similar structural phase transformations discovered in the $BaCeO_3$ material system [61]. Researchers also conducted similar experiments on the $BaCe_{0.85-x}Zr_xY_{0.15}O_{3-\delta}$ ($0.1 \leq x \leq 0.4$) and identified similar phase transitions [62]. The work confirmed, with synchrotron XRD and neutron powder diffraction, that the $BaCe_{0.75}Zr_{0.10}Y_{0.15}O_{3-\delta}$ material undergoes three structural phase changes as the temperature increases from room temperature to 700^{o}C;

$$BaCe_{0.75}Zr_{0.10}Y_{0.15}O_{3-\delta}$$

$$: \quad RT \xrightarrow[Monoclinic]{} 360^oC \xrightarrow[Orthorhombic]{} 640^oC \xrightarrow[Rhombohedral]{} 700^oC \xrightarrow[Cubic]{}$$

The work also revealed that a lowering of the transformation temperatures occurs with increasing zirconium content, due to the small ionic radius of the zirconium. In the $BaCe_{0.65}Zr_{0.20}Y_{0.15}O_{3-\delta}$ system the transition temperatures are lower;

$$BaCe_{0.65}Zr_{0.20}Y_{0.15}O_{3-\delta}$$

$$: \quad RT \xrightarrow[Monoclinic]{} 355^oC \xrightarrow[Orthorhombic]{} 490^oC \xrightarrow[Rhombohedral]{} 595^oC \xrightarrow[Cubic]{}$$

This work shows that the dopant in the $BaCeO_3$-based systems affects the temperatures at which the structural phase changes occur.

As we will see clearly in the next chapter, the $BaCeO_3$-based materials allow transport of protons, oxygen anions, and electronic defects, depending on temperature and atmosphere. Bonanos suggests that the change of majority charge carrier with temperature in the $BaCeO_3$-based systems is due to the structural phase transitions [25]. At lower temperatures, low symmetry phases exist in the $BaCeO_3$-based systems. In these low symmetry phases, different oxygen sites exist. The sites are not energetically or crystallographically equivalent, which decreases the mobility of oxygen vacancies (trapping). Conversely, at higher temperatures, the cubic structure forms in the $BaCeO_3$ doped material and all oxygen sites are equivalent. It is known that equivalent oxygen sites are beneficial for charge transport [43] and this could provide an explanation for protonic transport at low temperatures and oxygen anion transport at high temperatures [25].

In one study the $BaCeO_3$ system was doped with calcium in the A-site. A distortion, large enough to be detected by XRD, was verified and the distortion increased with increasing calcium, leading to a decrease in the oxygen anion conductivity [66]. It is assumed that the decreased symmetry led to unequal oxygen sites, which lead to trapping and reduction of oxygen anion conductivity. Also, as mentioned in chapter 2, the $SrCeO_3$ system has low symmetry and never reaches the cubic symmetry. The $SrCeO_3$-based system does not change from a majority proton conductor to a majority oxygen anion conductor like the $BaCeO_3$-based systems do with increasing temperature. Protonic defects are the majority charge carriers in this system at all temperatures under 1000^oC. The effect of Ca doping on the structure and the effect on the electrical properties in the $SrCeO_3$ system shows a strong correlation between the transport

properties and structure of the doped $BaCeO_3$ system. The effect of zirconium doping on the structural transition temperature of the BZCY system, also reveals the correlation between dopant and structure.

Therefore, we know that the Y^{3+} and Yb^{3+} dopants will have a unique effect on the structure of the BZCYYb material, which can also affect the transport properties. The disappearance of the split peaks around 600^{o}C in our HT-XRD data predicts that the structural phase transition temperatures in the BZCYYb material will be similar to the BZCY material system. Further work should be done with synchrotron XRD and neutron diffraction to determine the exact transition temperatures, so that the conductivity data of the BZCYYb material (from chapter 5) can be correlated to the transition temperatures. If the temperature of transition from proton to oxygen anion majority carrier is verified to be determined by the structural phase transformation temperatures, the doped $BaCeO_3$-based systems can be tailored for applications which require proton conduction or for applications which require oxygen anion conduction.

The effect of NiO on the BZCYYb material is not fully understood. There is no observable peak splitting in the XRD patterns of the NiO-BZCYYb mixture and the widths of the characteristic perovskite peaks reduce with increased temperature. The NiO may act to stabilize the high symmetry rhombohedral or cubic phase of the BZCYYb system at RT. Therefore NiO addition could decrease fabrication temperatures and increase mechanical stability during thermal cycling of IT-SOFC stacks. Further work must be done to determine the effect of NiO addition on the structure of the material.

CHAPTER 4

MIXED IONIC (PROTONIC AND OXYGEN ANION) AND ELECTRONIC CONDUCTION IN $BaCeO_3$- BASED PEROVSKITE MATERIAL SYSTEMS

4.1 Protonic and Electronic Defects in the $BaCeO_3$ system

Oxygen defects are formed for charge compensation in the $BaCeO_3$-based systems due to extrinsic doping, as seen in equation 18. Protonic and electronic defects form in the $BaCeO_3$-based system by the oxygen vacancies created during the trivalent doping of the Ce^{4+} site. Protonic defects form according to the hydration reaction (19).

$$H_2O + O_O^X + V_{\ddot{O}} \leftrightarrow 2OH^{\cdot} \quad (19)$$

In water containing environments, oxygen vacancies are filled by hydroxide ions and the extra proton, from the water molecule, bonds with a lattice oxygen [43]. The proton then diffuses from one lattice oxygen to the next. The incorporation of water into the $BaCeO_3$-based system can be quantified by the weight increase associated with the water incorporation. Hydration isobars for the $BaCeO_3$-based systems can be measured by TGA analysis at temperatures relevant to SOFC operation to understand the energy required for hydration and the concentration of protonic defects in the system at specific temperatures. Kreuer has done much work in this area to understand high temperature proton conduction in perovskite oxides and the effect of dopants on the proton conduction [43].

As mentioned, the crystal symmetry of the material effects the defect mobility. The symmetry affects the mobility of protonic defects as well as oxygen defects. As before, decreased symmetry can lead to two lattice oxygen sites with different electron densities. Though not as strongly as the oxygen anion transport, the different oxygen sites also affects the proton

transport. The difference in electron density of the lattice oxygen can lead to different binding energies for the proton at the two oxygen lattice sites. Experimental findings of higher activation enthalpy and lower conductivity in the $SrCeO_3$-based orthorhombic systems when compared to the $BaCeO_3$-based cubic systems support this theory [19, 43]. Therefore dopants which decrease the symmetry of the material system should decrease the conductivity. However, in direct contradiction, in the $BaZrO_3$-based system, dopants (In^{3+}, Sc^{3+}) with ionic radii matching the Zr^{4+} ion show higher activation enthalpies than Y^{3+}, although Y^{3+} doped in the B-site causes tetragonal distortions in the host structure [43]. Although the Y^{3+} dopant slightly lowers the symmetry of the structure, the Y^{3+} doped system has higher conductivity than the systems with dopants of similar ionic radii to the Zr^{4+} ion. Kreuer explains that the chemical nature of the dopant plays a role in the proton transport as well. Because the yttrium dopant leaves the chemical environment of the coordinating oxygen practically unchanged it does not interfere with proton transport and leads to higher conductivies and lower activation enthalpies [43]. Therefore both the chemical nature and size of the dopant must both be considered to understand the dopant effect on defect transport.

The plots in Figure 16 are simulated defect concentrations in rare earth doped cerate perovskite proton conductors with respect to PO_2 and PH_2O. The B-site trivalent dopant amount for the simulation is 10%. The defect concentrations in real systems will vary from the simulated values; however, the plots give a good idea of the relationships of the concentrations of the coexisting defects [67].

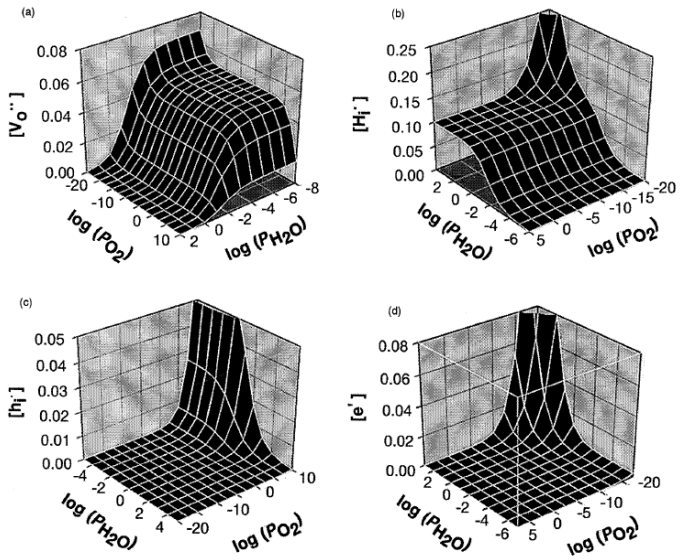

Figure 16: Defect concentrations for a logarithmically spaced grid of PO_2 and PH_2O for the case $[M_B']=0.1$. (a) oxide ion vacancies, (b) protons, (c) holes and (d) electrons. Partial pressures are in atm. The plateaus visible in (a) and (b) correspond to intrinsic charge compensation regimes [67].

4.2 Proton Transfer Mechanism in $BaCeO_3$ and $SrCeO_3$ Material Systems

A study of the proton transfer mechanism in the $SrCeO_3$ and $BaCeO_3$ doped systems was published by Kreuer. During protonic conduction in the $BaCeO_3$ and $SrCeO_3$ systems, the proton moves from oxygen site to oxygen site, forming hydrogen bonds with the oxygen at each lattice site. Figure 17 illustrates the two mechanisms by which proton conduction occurs.

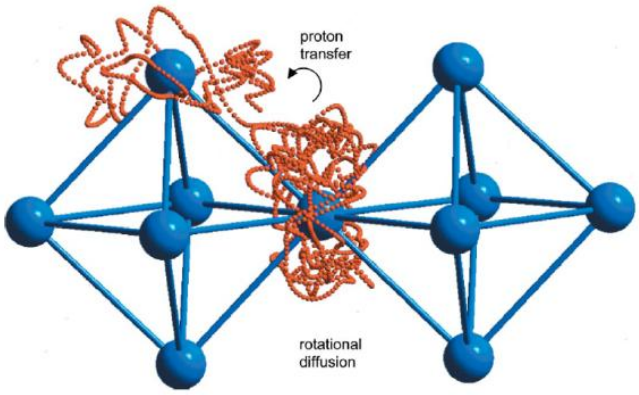

Figure 17: Two mechanisms by which proton transport occurs in $BaCeO_3$; rotational (around a lattice oxygen) and translational (proton transfer from one lattice oxygen to another) diffusion (blue: O^{2-}, orange: trace of proton path from MD simulation) [43]

For protonic conduction there is a rotational diffusion component of the defect around the lattice oxygen and a translational diffusion of the proton towards a neighboring oxygen ion. The rotational diffusion of the defect is limited by the strong hydrogen bond that forms between the proton and the lattice oxygen, as the rotation requires the breaking of bonds with neighboring oxygen. However, this energy is balanced by the extra energy necessary to deform the lattice to allow the lattice ions to sit close enough for hydrogen bonding to occur. Large separations between the proton and the lattice oxygen favor rotational diffusion, whereas a short distance between the lattice oxygen favors the translational diffusion of the proton. Kreuer also suggests that further simulation data shows that there is a repulsive interaction between the proton and the B-site cation in the perovskite octahedra, causing the proton to move not in a straight line between the neighboring oxygen, but bending the path and adding to the barrier for proton transfer. This idea provides explanation for the lower proton mobility in $A^{1+}B^{5+}O_3$ perovskites as compared to the $A^{2+}B^{4+}O_3$ perovskites. The high coordination of the oxygen in the perovskite structure is generally advantageous for proton conduction because it means that the proton is bonded to many other lattice oxygen. The angle between the bonds is small when coordination

number is high, therefore reducing the energy necessary for breaking the bonds during the rotational diffusion process [43].

4.3 Determination of Transference Numbers by the Concentration Cell - OCV Method

Potentiometry, first proposed by Wagner [68] for oxygen ion conductors, is used to determine the transference numbers of an electrolyte. A gradient in PO_2 is maintained at two identical electrodes (I and II) separated by the electrolyte and the open circuit voltage (OCV) of the concentration cell is measured. The OCV of the cell with identical, reversible electrodes at equilibrium is given by equation 21.

$$OCV = \frac{RT}{4F} \int_{I}^{II} t_{ion}\, d(\ln P_{O_2}) \tag{21}$$

In order to integrate equation 21, the dependence of t_{ion} on the PO_2 must be known. However, one can assume that the t_{ion} does not vary greatly over the PO_2 range, and t_{ion} can represent a mean value over the oxygen partial pressure range [69]. The OCV after integration, for an oxygen anion and electronic conductor, is given in equation 22.

$$OCV = t_{ion} \cdot E_{Nernst} = t_{ion} \cdot \frac{RT}{4F} ln \frac{P_{O_2}^{II}}{P_{O_2}^{I}} \tag{22}$$

The ionic transference number for the oxygen anion and electronic conductor, t_{ion}, can be approximated by the ratio of the measured OCV to the Nernst potential at equilibrium. In essence, the electronic conduction in the oxide partially shorts the circuit between the electrodes and lowers the OCV. Therefore the electronic transference number, $t_{e^-} = 1 - t_{ion}$. However, this equation does not hold if the oxide also transports other species [70].

In a hydrogen concentration cell, a gradient in partial pressures of hydrogen at two identical electrodes separated by a proton conductor generates a measurable OCV [71]. For a protonic and electronic conductor the OCV is related to the hydrogen partial pressures by equation 23, and the protonic transference number, t_{H^+}, is again an average over the hydrogen partial pressure range [70].If the material also conducts ionic species other than protons, such as oxygen vacancies, equation 23 cannot be used to determine the protonic transport number.

$$OCV = t_{H^+} \cdot \frac{RT}{2F} ln \frac{P_{H_2}^{II}}{P_{H_2}^{I}} \tag{23}$$

When the oxygen concentration cell or the hydrogen concentration cell contains water at each electrode, the electrodes are both in a H_2, O_2 and H_2O containing environment, due to the thermodynamic equilibrium of the water reaction 24.

$$H_2 + \frac{1}{2} O_2 = H_2O \tag{24}$$

Equation 23, can be rewritten in terms of the PO_2 and PH_2O for an O_2 and H_2O concentration cell (equation 25),

$$OCV = t_{H^+} \cdot \frac{RT}{4F} ln \frac{P_{O_2}^{II}}{P_{O_2}^{I}} - t_{H^+} \cdot \frac{RT}{2F} ln \frac{P_{H_2O}^{II}}{P_{H_2O}^{I}} \tag{25}$$

Therefore when water is added to the H_2 or O_2 concentration cells, defects formed in the O_2 atmosphere and those in a H_2 containing atmosphere can all contribute to the conduction in the system. If only protonic and electronic defects form, even in oxygen containing environments, then equation 25 is valid for determining the protonic transference number. However, if protonic, electronic, and oxygen defects form, the differentiation in transference number for each defect species is not possible with these equations [70].

For a material which conducts protons, oxygen anions, and electrons, we can differentiate the transference number of each type of charge carrier by relating the electrode reactions to the voltage measured at the electrodes under an open circuit condition.

To determine the transference numbers of all charge carrying species in a mixed conductor, the oxide is sealed so that it separates two compartments (1,2) with well defined PO_2, PH_2, and PH_2O at each electrode. The electrodes are of the same metal and the experiment is conducted when the gases are in electrochemical equilibrium with the corresponding electrodes and therefore in equilibrium with the surfaces of the oxide. The voltage between the two electrodes is measured under an open circuit condition (OCV), when no current passes through the oxide[70].

Sujita [70] uses the species flux to relate the mobility, concentration, and charge of the species to the electrical potential gradient between the electrodes. The gradient in electrical potential across the oxide is given in equation 26.

$$\nabla \emptyset = -\frac{RT}{F}\sum_{k}\frac{t_k \cdot \nabla \ln c_k}{z_k} \tag{26}$$

By assuming a constant transport number across the thickness of the oxide and an isothermal system, the right side of equation 26 can be solved and the potential difference across the oxide, $\emptyset_{II} - \emptyset_{I}$, is determined. The voltage measured between the identical electrodes is equal to the difference in electrochemical potential of electrons at each electrode which is given by equation 27.

$$E_{II-I} = (\emptyset_{II} - \emptyset_{I}) - \frac{RT}{F}\Delta \ln c_{e^-} \tag{27}$$

By combining equation 27 and the integral of equation 26 we get equation 28.

$$E_{II-I} = -\frac{RT}{F}\Delta \ln c_{e^-} \frac{RT}{F}\sum_k \frac{t_k}{z_k}\Delta lnc_k \quad (28)$$

Using the reactions for ionic species formation at the electrodes,

$$H_2 \leftrightarrow 2H^{\cdot} + 2e^- \quad (29)$$

$$\frac{1}{2}O_2 + 2e' = O^{2-} \quad (30)$$

the terms containing c_{e^-} cancel and (assuming the protonic defects are positive) we come to equation 31,

$$E_{II-I} = t_{O^{2-}} \frac{RT}{4F} ln \frac{P_{O_2}^{II}}{P_{O_2}^{I}} - t_{H^+} \frac{RT}{2F} ln \frac{P_{H_2}^{II}}{P_{H_2}^{I}} \quad (31)$$

when the partial pressures of the reacting gases are used in place of the concentrations. Equation 24 can be used to rewrite equation 31 in terms of water vapor partial pressures [70].

$$E_{II-I} = t_{ion} \frac{RT}{4F} ln \frac{P_{O_2}^{II}}{P_{O_2}^{I}} - t_{H^+} \frac{RT}{2F} ln \frac{P_{H_2O}^{II}}{P_{H_2O}^{I}} \quad (32)$$

$$E_{II-I} = -t_{ion} \frac{RT}{2F} ln \frac{P_{H_2}^{II}}{P_{H_2}^{I}} + t_{O^{2-}} \frac{RT}{2F} ln \frac{P_{H_2O}^{II}}{P_{H_2O}^{I}} \quad (33)$$

Concentration cells with specific PO_2, PH_2, and PH_2O can be setup and the $t_{O^{2-}}$ and the t_{H^+} can be determined. The concentration cell - OCV method has been used to characterize the $BaCe_{0.95}Y_{0.05}O_{3-\alpha}$ system under H_2/H_2O and O_2/H_2O conditions [72] as well as many other mixed conductors.

The transference numbers of the charge carrying species in the BZCYYb material are important for several reasons. When used in SOFC systems, the amount of charge carried by protonic defects and oxygen defects effects where the water for the fuel cell reactions is formed,

at the cathode or the anode. The electrode at which the water forms affects the efficiency of the cell and the ability of the cell to internally reform hydrocarbon fuels. Also, high electronic defect contribution decreases the OCV of the SOFC and decreases cell efficiency. For hydrogen separation membranes, hydrogen passes through the membrane via protonic defects. Therefore, a material with a high proton transference number at operating conditions is optimal. The portion of electronic charge carriers is also important for hydrogen separation membranes.

4.4 Experimental

4.4.1 Electrical Conductivity Testing of BZCYYb

Electrochemical Impedance spectroscopy (EIS) was used to determine the bulk resistance of the sintered BZCYYb pellets in H_2, O_2 and H_2O atmospheres which are important for SOFC application. EIS separates the total ohmic resistance of the BZCYYb (bulk resistance, R_b) from the total cell resistance. The intercept with the real axis is the bulk resistance, due to the BZCYYb, and is used in equation 34 to determine the conductivity. Silver (Ag) slurry was tape cast and Ag electrodes were punched (d=1/4 in.) and applied to both sides of the sintered BZCYYb pellets using an Ag suspension for intimate contact. After application of the electrodes, the pellets were fired at 700^{o}C for 2 hours in ambient air. Figure 18A shows the Ag electrode on the BZCYYb pellet after testing. The left portion of the image in Figure 18A shows the Ag electrode delaminated from the BZCYYb pellet after SEM sample preparation. The delaminated section is shown to represent the thickness and porosity of the Ag electrode and the right side shows good contact with the pellet. Figure 18B shows the Ag interlayer created by the Ag suspension which is used to attach the tape cast electrode to the sample. The interlayer increases the contact area between the BZCYYb pellet and the Ag tape cast electrode. Silver wires were

attached to the fired Ag electrodes with Ag paste (Heareus) for current collection. The pellets were tested in controlled atmospheres of H_2, O_2, or H_2O and in the temperature range of 550°C-750°C. The H_2O partial pressure was controlled by passing the inlet gas through H_2O in a constant 25°C bath. This adds approximately 3% H_2O to the fuel stream.

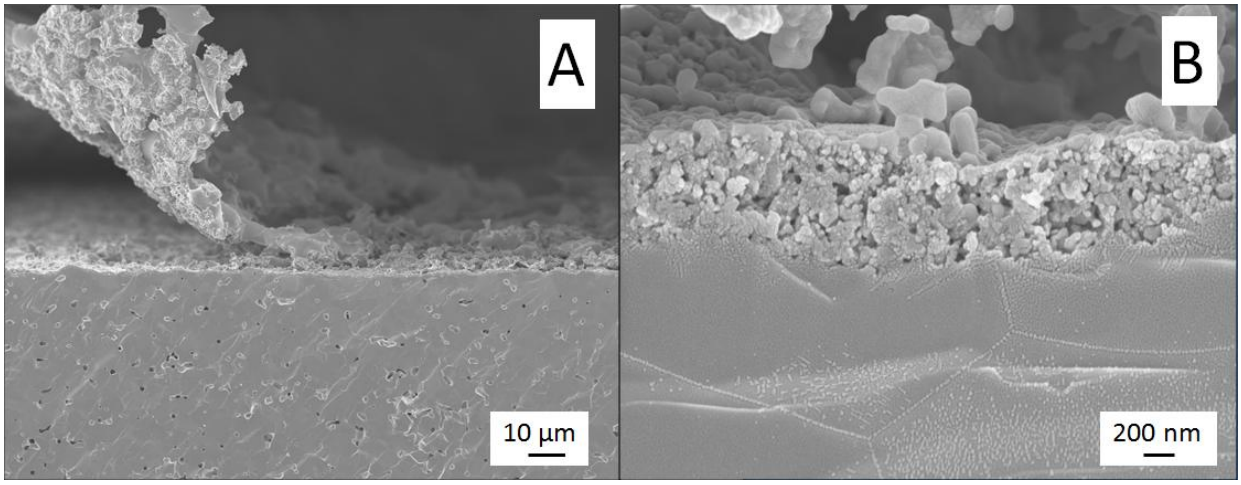

Figure 18: Ag | BZCYYb | Ag cell with A.) tape cast Ag electrode pelled (left side) and well adhered (right side) and B.) Ag interlayer.

Typical EIS data are shown in Figure 19. The bulk resistance increases as the temperature decreases.

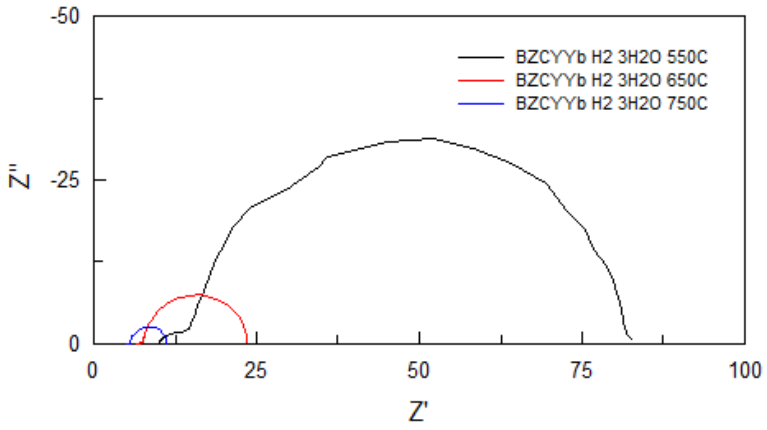

Figure 19: Impedance Spectroscopy data for the Ag | BZCYYb | Ag cell under 3%H_2O/H_2 conditions at 550°C, 650°C, and 750°C.

The bulk resistance of the BZCYYb pellets was used in equation 34, along with the physical dimensions of the pellet, to determine the bulk conductivity.

$$\sigma = \frac{1}{R_b} * \frac{L}{S} \tag{34}$$

L is the thickness of the samples and S is the area of the electrode. The activation energy is estimated from the slope of the Arrhenius plot for conductivity (plotted ln(σT) vs. 1/T) (equation 35).

$$\sigma T = \sigma_o \exp\left(\frac{-E_a}{RT}\right) \tag{35}$$

4.4.2 Concentration Cell-OCV Testing of BZCYYb

Platinum electrodes (d=1/4 in.) were applied to BZCYYb pellets for concentration cell testing. Platinum slurry (Heareus) was brush coated onto the BZCYYb sintered pellets and fired at 900^{o}C for 2 hours. Platinum mesh and wire was attached with platinum paste and used for current collection. Concentration cells were tested using the experimental setup displayed in Figure 20. The Pt│BZCYYb│Pt cell was sealed (Ceramabond 552, Aremco) onto an alumina testing fixture. The fixture was covered with a quartz tube to control the testing atmosphere. H_2/H_2O and O_2/H_2O cells were tested to determine the transference numbers under SOFC anode and cathode, respectively, conditions. The flowrate was controlled to 60 cm^3/min on each side of the cell. The partial pressure of H_2O was controlled by passing the inlet gas through a constant temperature bath (25^{o}C, 40^{o}C). OCV measurements were recorded using an Arbin multi-channel electrochemical testing system (MSTAT) after the system equilibrated.

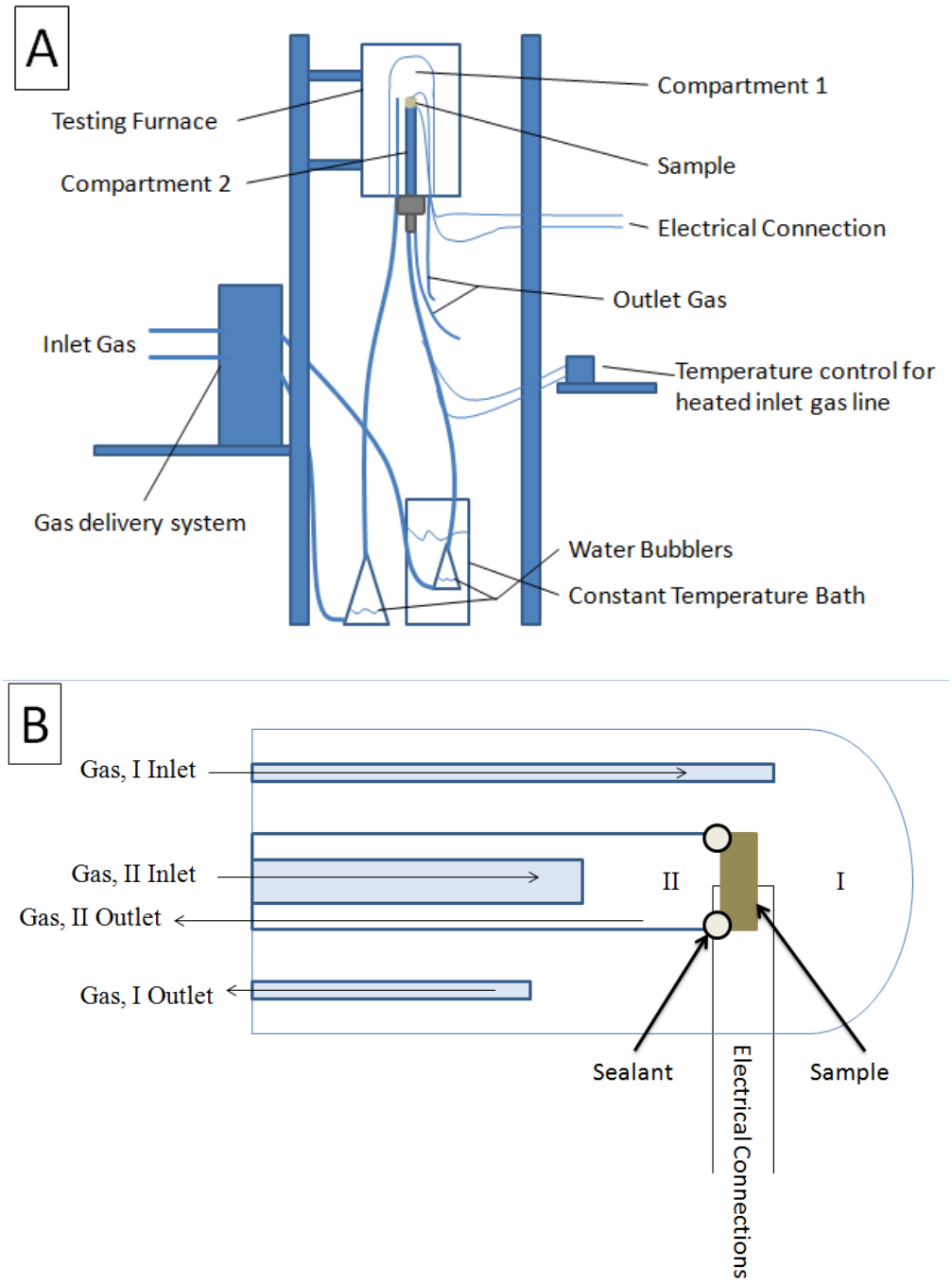

Figure 20: A.) Concentration Cell –OCV technique experimental setup and B.) Concentration Cell – OCV technique testing fixture

The Ceramabond 552 (Aremco) sealant used for attaching the Pt | BZCYYB | Pt cell to the testing fixture does not form a completely dense barrier between "Compartment 1" and

"Compartment 2". The SEM image in Figure 21 reveals the significant porosity of the sealant after testing.

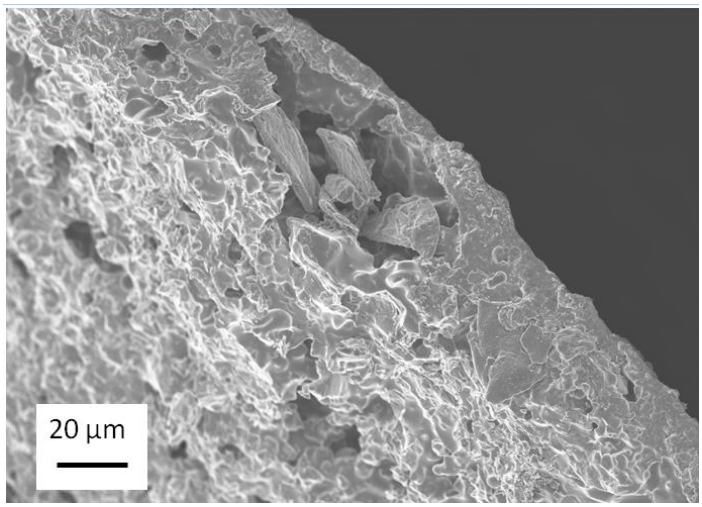

Figure 21: Cross-sectional view of porous Ceramabond 552 (Aremco) sealant after testing.

Therefore, corrections were made in the OCV data for the leakage due to the sealant. Sintered yttria-stabilized zirconia pellets were used to determine the correction factor for the leakage. YSZ was chosen because the material has no electronic conduction, therefore, changes in OCV due to electronic conduction would not be included in the correction factor. The measured OCV was compared to the ideal OCV, calculated with the ionic transference number equal to one, $t_{ion} = 1$. The leakage correction factor and data are in Table 1.

Table 1: YSZ Concentration Cell Data, II, O_2+3.13%H_2O, Pt | YSZ | Pt, Ar + 1% O_2 + 3.13% H_2O, I

T (C)	OCV (V)	t_{ion}	$t_{electronic}$	Ideal OCV (V)	Leakage Correction Factor (Ideal/Measured)
800	0.0977	0.92	0.08	0.1057	1.082
750	0.0933	0.93	0.07	0.1008	1.08
700	0.0889	0.93	0.07	0.0959	1.078
650	0.0845	0.93	0.07	0.0909	1.076
600	0.08	0.93	0.07	0.086	1.075

The transference numbers of the BZCYYb were calculated in O_2/H_2O atmospheres with the following two concentration cells:

O_2/H_2O Cell 1: $$II, O_2 + 3.13\%H_2O, Pt \,|\, BZCYYb \,|\, Pt, 1\%O_2 + 3.13\%H_2O + Ar, I$$

O_2/H_2O Cell 2: $$II, O_2 + 7.28\%H_2O, Pt \,|\, BZCYYb \,|\, Pt, 1\%O_2 + 3.13\%H_2O + Ar, I$$

Equation 36 is used to relate the OCV of the concentration cell to the transference numbers and the PO_2 and PH_2O for the O_2/H_2O concentration cells

$$E_{II-I} = t_{ion}\frac{RT}{4F}ln\frac{P_{O_2}^{II}}{P_{O_2}^{I}} - t_{H^+}\frac{RT}{2F}ln\frac{P_{H_2O}^{II}}{P_{H_2O}^{I}} \quad (36)$$

In Cell1, the absence of a gradient in PH_2O makes it possible to determine the t_{ion} due to the gradient of PO_2 from the equilibrium value of the OCV of the concentration cell. The electronic transference number can immediately be calculated as well. Next, in Cell 2, the gradient in PO_2 is not changed, however, a gradient in PH_2O is created in the system. The equilibrium OCV value is recorded and the t_{ion} value from Cell 1 is used to calculate t_{H^+}. The protonic transference number, t_{H^+}, can then easily be determined.

Similarly, in the H_2/H_2O atmospheres, the transference numbers were determined with the following two concentration cells:

H_2/H_2O Cell 1: $$II, H_2 + 3.13\%H_2O, Pt \,|\, BZCYYb \,|\, Pt, 4\%H_2 + 3.13\%H_2O + Ar, I$$

H_2/H_2O Cell 2: $$II, H_2 + 7.28\%H_2O, Pt \,|\, BZCYYb \,|\, Pt, 4\%H_2 + 3.13\%H_2O + Ar, I$$

Equation 37 is used to determine the transference numbers.

$$E_{II-I} = -t_{ion}\frac{RT}{2F}ln\frac{P_{H_2}^{II}}{P_{H_2}^{I}} + t_{O^{2-}}\frac{RT}{2F}ln\frac{P_{H_2O}^{II}}{P_{H_2O}^{I}} \quad (37)$$

4.5 Results

4.5.1 Conductivity

Impedance spectra were collected for the BZCYYb sintered pellet with Ag electrodes in each atmosphere, H_2/3%H_2O, O_2/3%H_2O, and ambient air from 550°C – 750°C. The atmospheres were used for testing to understand the conductivity of the BZCYYb material under anode and cathode conditions of a proton conducting SOFC. The conductivity for the BZCYYb sintered pellets in each of the atmospheres is graphed in Figure 22. The BZCYYb conductivity is highest in the O_2/H_2O atmosphere above 600°C. However, the high activation energy for oxygen anion conduction causes the conductivity to decrease more quickly than the conductivity in the H_2/H_2O environment, resulting in higher conductivity below 600°C in the H_2/H_2O environment. The activation energy for the O_2/H_2O atmosphere, where a mixture of oxygen anion and proton conduction occurs, is approximately 0.44eV. For the H_2/H_2O atmosphere, where proton conductivity dominates, the activation energy is approximately 0.30eV. Because the activation energy for protonic conduction is less than oxygen anion conduction, the activation energy is smaller in the H_2/H_2O environment. The conductivity for BZCYYb in an ambient air atmosphere is also plotted and the activation energy for conduction is similar to the result in the O_2/H_2O environment. The conductivity is lower in ambient air due to the decreased PO_2 in the testing atmosphere.

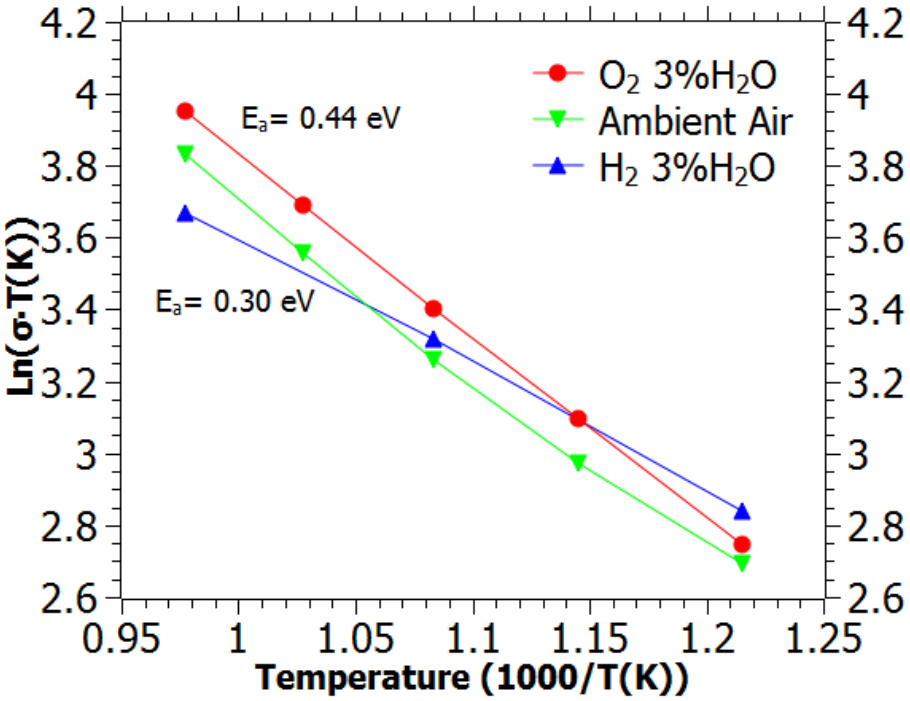

Figure 22: Conductivity of BZCYYb pellets in O_2/3%H_2O, H_2/3%H_2O, and Ambient Air atmospheres

Equation 20 revealed that electronic defects can form in the BZCYYb material at high PO_2 in a dry atmosphere. Oxygen (gas) fills oxygen vacancies and electron holes form for charge compensation. However, in atmospheres with significant PH_2O, the oxygen vacancies are filled with protonic defects (equation 19) and the electronic conductivity should be reduced significantly. To understand the difference of dry/O_2 and 3%H_2O/O_2 atmospheres on the BZCYYb conductivity, the BZCYYb pellet with Ag electrodes was tested in an atmosphere in which the PH_2O could be controlled. The pellet was heated to 650^oC and a 0.1V DC bias was set-up across the pellet. The current was measured as the atmosphere was switched from dry to wet. The results are shown in Figure 23. The current is higher in the dry/O_2 atmosphere and then drops as the atmosphere is switched to 3%H_2O/O_2. The current increases in the atmosphere with no H_2O, as expected with the formation of electron holes in this environment.

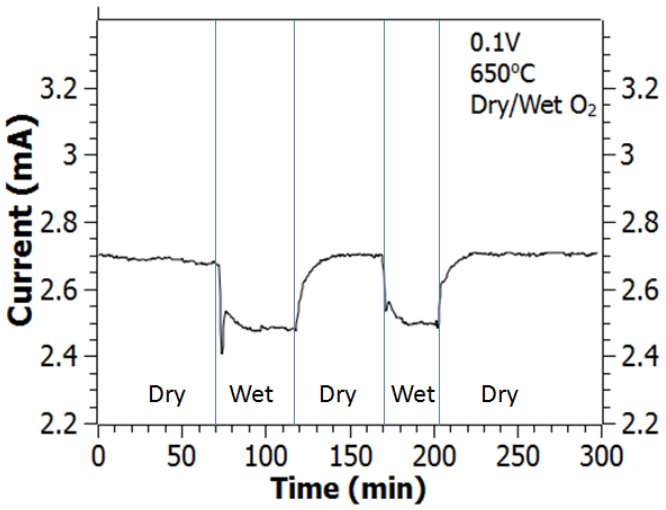

Figure 23: Change in current due to change in PH_2O for a BZCYYb pellet in O_2 atmosphere at 650°C and under 0.1V DC bias

4.5.2 Transference Numbers

4.5.2.1 O_2/H_2O Concentration Cell

The OCV measurements for the O_2/H_2O cells were taken as described in the experimental section using the following concentration cells:

$$\text{Cell 1: } II, O_2 + 3.13\%H_2O, Pt \,|\, BZCYYb \,|\, Pt, 1\%O_2 + 3.13\%H_2O + Ar, I$$

$$\text{Cell 2: } II, O_2 + 7.28\%H_2O, Pt \,|\, BZCYYb \,|\, Pt, 1\%O_2 + 3.13\%H_2O + Ar, I$$

In Table 2, the OCV measurements of the cells under O_2/H_2O atmosphere, after reaching equilibrium, are recorded. The calculated transference numbers for the O_2/H_2O concentration cells are presented in Figure 24. The OCV values for Cell 1 increase with decreasing temperature from 800°C to 650°C. A peak occurs at 650°C and the OCV drops at 600°C. Cell 2 OCV values are similar but slightly lower, due to the increase in protonic defects due to the increase in PH_2O on the low PO_2 side. The initial increase in OCV, for both cells, is due to the decrease in

electronic conductivity as temperature decreases, consistent with electronic conductivity in ceramics. The OCV peaks at 650°C, and then the OCV decreases at 600°C due to the increase in protonic conductivity at lower temperatures. The positive charge of the protonic charge carriers decreases the OCV of the concentration cell, whereas the negative oxygen anion charge carriers increase the OCV of the cell.

Table 2: OCV data from BZCYYb O_2/H_2O Concentration Cells

Temperature	OCV (mV)	
(°C)	Cell 1	Cell 2
800	46.96	43.92
750	48.61	44.69
700	50.25	45.16
650	50.58	43.69
600	48.81	41.68

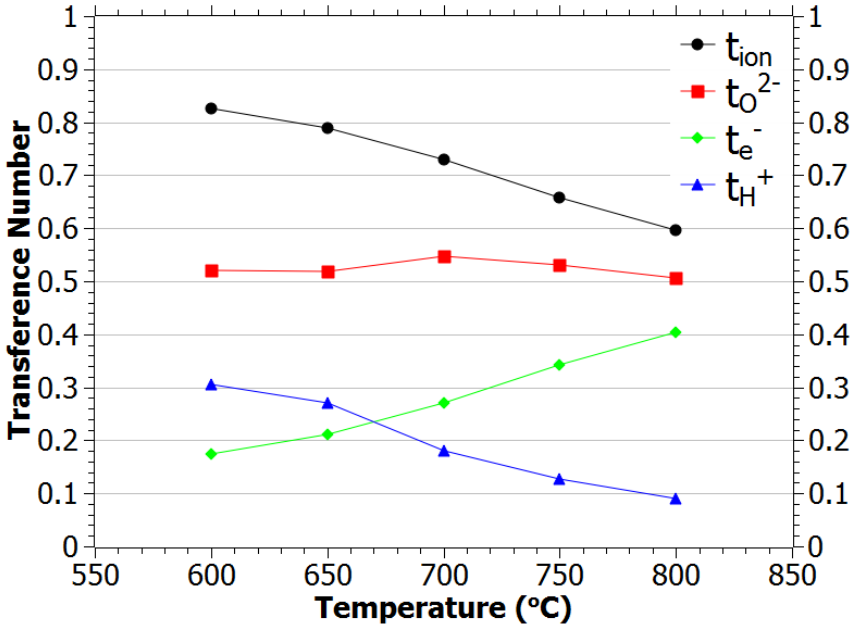

Figure 24: Transference numbers for BZCYYb pellet in O_2/H_2O atmosphere calculated with the concentration cell – OCV method

As temperature decreases from 800°C to 600°C, the transference number for protonic defects increases while the transference number of the oxygen anion defects remains the same. The transference number for electronic defects decreases dramatically with the temperature decrease. The O_2/H_2O concentration cell atmosphere imitates the conditions at the cathode side of a proton conducting SOFC.

4.5.2.2 H_2/H_2O Concentration Cell

Likewise, the H_2/H_2O concentration cell OCV measurements were taken using Cells 1 and 2 below.

Cell 1: $II, H_2 + \ 3.13\%H_2O, Pt \mid BZCYYb \mid Pt, 4\%H_2 + 3.13\%H_2O + Ar, I$

Cell 2: $II, H_2 + \ 7.28\%H_2O, Pt \mid BZCYYb \mid Pt, 4\%H_2 + 3.13\%H_2O + Ar, I$

In Table 3, the equilibrium OCV values of the cells under H_2/H_2O atmosphere at 800°C, 650°C, and 600°C are recorded. The calculated transference numbers are graphed in Figure 25. With the orientation of the cells used in this experiment, the sign of the OCV measurement is opposite of the O_2/H_2O concentration cell measurements due to the opposite sign of the charge carrier. The trends in the OCV values are similar to the O_2/H_2O concentration cells, but negative, due to majority protonic conductivity.

Table 3: OCV data from BZCYYb H_2/H_2O Concentration Cells

Temperature	OCV (mV)	
(°C)	Cell 1	Cell 2
800	-91.98	-88.70
650	-107.62	-105.21
600	-104.29	-102.87

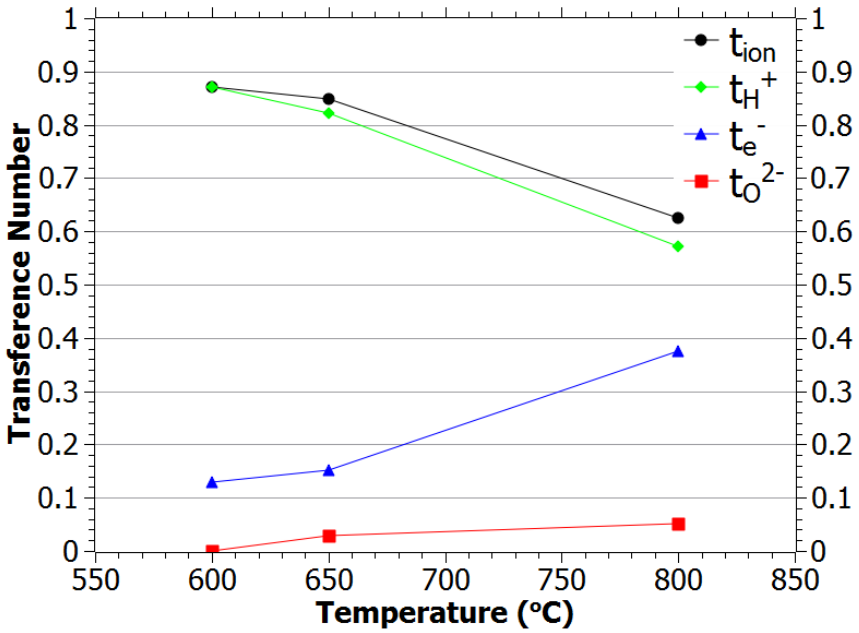

Figure 25: Transference numbers for BZCYYb pellet in H_2/H_2O atmosphere calculated with the concentration cell – OCV method

The transference number data for the H_2/H_2O concentration cells reveals majority proton conductivity at all tested temperatures. Very little oxygen anion conductivity is present due to the small partial pressure of oxygen present and the formation of protonic defects with water by the hydration reaction (equation 19) which consumes oxygen vacancies. The electronic conductivity also decreases with decreasing temperature, as in the O_2/H_2O concentration cell. The H_2/H_2O concentration cell atmosphere imitates the conditions at the anode side of a proton conducting SOFC.

4.6 Discussion

The conductivity and concentration cell - OCV data in H_2/H_2O and O_2/H_2O atmospheres reveals the significant changes in charge carrier in the anode and cathode environments of the proton conducting SOFC. The BZCYYb is a mixed ionic (proton and oxygen anion) and electronic conductor.

Although the conductivities reported in this work and in the literature are heavily influenced by processing conditions, sample preparation, and measurement techniques, our conductivity data is in good agreement with the literature reports for $BaCeO_3$-based systems and the calculated activation energies are reasonable for protonic and oxygen anion conduction. Higher activation energy in the $3\%H_2O/O_2$ atmosphere is a result of majority oxygen anion charge carriers. Oxygen anion conduction is reported to have higher activation energy than proton conduction and our calculated results agree. Also, the crossover temperature of the conductivity in the O_2 containing and H_2 containing environments is near the temperature that the peaks are no longer split in the HT-XRD data of chapter 3, indicating a possible connection between the structural symmetry and the conductivity.

The significant contribution of oxygen anion and protonic conduction dictates that water from the fuel cell reaction will form at both electrodes. This makes the BZCYYb material useful because it allows for the possibility of internal reforming of hydrocarbon fuels at the anode, as well as an increase in SOFC efficiency due to the balance of water forming at the cathode.

The electronic transference numbers, determined by the concentration cell - OCV method, are high in both atmospheres. In the next chapter, we fabricated full SOFCs based on BZCYYb and tested performance, however, to better understand the ionic and electronic transference data of this chapter, we tested the OCV of a full SOFC based on BZCYYb. In Figure 26 the theoretical OCV of the cell based on $3\%H_2O/H_2$ fuel and $3\%H_2O/O_2$ oxidant is graphed, as well as the measured OCV values. The theoretical OCV value was calculated using the equilibrium constant, k, calculated from gas phase thermochemistry data sets [73].

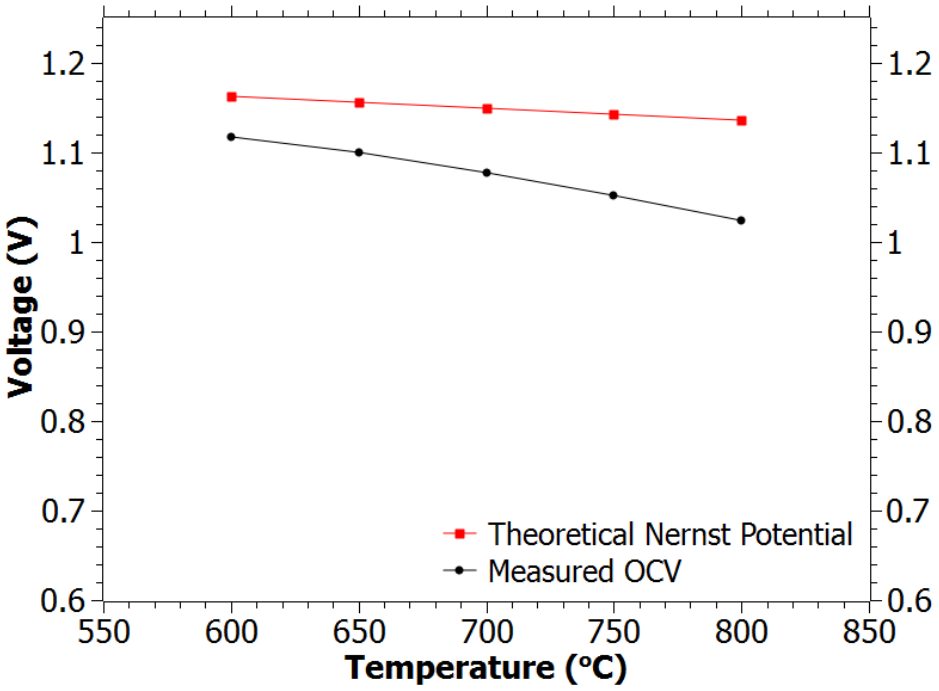

Figure 26: Measured and theoretical OCV of Ni-BZCYYB/BZCYYb/LSCF-BZCYYb SOFC with 3%H_2O/H_2 fuel and 3%H_2O/O_2 oxidant from 600°C – 800°C

Surprisingly, the theoretical OCV values are only 11% and 4% greater than the measured OCV values at 800°C and 600°C, respectively. The deviation from the theoretical value can be due to many factors but the majority of the decrease is due to electronic conductivity in the electrolyte, in this case BZCYYb. Electronic conductivity "shorts" the SOFC and decreases the OCV value from the theoretical Nernst potential, calculated from the partial pressures of gases at each electrode. The OCV of the SOFC reveals that under fuel cell conditions, the electronic transference numbers can be no greater than 0.11 at 800°C and 0.04 at 600°C. However, in the transference number data, the electronic transference numbers are much larger in both atmospheres. Therefore, either the combination of both atmospheres under fuel cell operating conditions work synergistically to decrease the electronic charge carriers in the system, or the concentration cell - OCV method (which is used abundantly in the literature) does not accurately

indicate the electronic transference numbers of the system. It is not immediately apparent how to reconcile the data.

However, one aspect of the ionic transport is not accounted for in the concentration cell - OCV method. This may explain the high electronic transference numbers determined by the concentration cell - OCV method. As we know, H_2, O_2, and H_2O are in thermodynamic equilibrium in all of the atmospheres tested. Although H_2 is not supplied in the O_2/H_2O cell and O_2 is not supplied in the H_2/H_2O cell, small amounts will be present. Therefore, all three gases are present in each of the tests. For example, the calculated [73] PH_2 values for compartment 2 and compartment 1 of the O_2/H_2O concentration cell 1 are listed in Table 4.

Table 4: Equilibrium PH_2 in O_2/H_2O concentration cell

T (°C)	PH_2, II	PH_2, I
800	2.11E-11	2.07E-10
750	5.41E-12	5.33E-11
700	1.21E-12	1.19E-11
650	2.31E-13	2.27E-12
600	3.65E-14	3.59E-13

A gradient in PH_2 is present in the cell, however, this gradient is not accounted for in equation 36. The PH_2 gradient will further reduce the OCV of the cell. However, when equation 36 is used, the reduction of OCV, due to the PH_2 gradient is accounted for by a decrease in the ionic transference number, which automatically increases t_e-. Therefore, the proton conductivity in the cell, due to the PH_2 gradient, is mistaken for electronic conductivity. Therefore, the electronic transfer number is artificially increased due to the concentration cell - OCV technique. A different gradient in PH_2 is present in the O_2/H_2O concentration cell 2. Also, a similar

unaccounted gradient in PO_2 is present in the H_2/H_2O concentration cells, which increases the calculated electronic transference number.

CHAPTER 5

PROTON CONDUCTING SOFC ANODE MICROSTRUCTURE

5.1 Introduction

SOFC anodes are commonly composed of nickel, which is inexpensive but electrocatalytically active for hydrogen oxidation at SOFC operating temperatures [74]. Cermet anodes are fabricated by mixing NiO and an ionically conducting oxide (e.g., an electrolyte) followed by reduction of NiO to Ni(metal) upon exposure to a fuel during the first hours of SOFC operation. Reduction of NiO creates porosity in the anode which is needed for gas-phase diffusion. The contiguous nickel metal creates electronic conduction pathways throughout the anode. Both porosity and electronic conduction are critical for the functions of a SOFC anode. The ion-conducting phase of the cermet anode, often identical to the electrolyte material of the cell, forms a framework primarily responsible for structural support of the cell, maintenance of anode microstructure throughout the lifetime of cell operations, intimate contact with the dense electrolyte, and extension of the triple phase boundaries (gas, electronic conductor, ionic conductor) into the porous anode to increase the number of active sites for fuel oxidation [75, 76]. Due to the difference of charge carrier in proton conducting and oxygen anion conducting SOFCs, anodes of different microstructures must be used in each type of SOFC to optimize performance. However, few studies [77, 78] focus on the effect of anode microstructure on proton conducting SOFC performance.

The state-of-the-art YSZ based oxygen anion conducting SOFC has been widely studied. The effect of microstructure (such as porosity, pore size, and Ni to YSZ ratio) of a Ni-YSZ cermet anode on fuel cell performance has been systematically investigated [79-81]. For

example, the optimal porosity in the Ni-YSZ cermet anode is higher than the porosity that is formed simply from the reduction of NiO during cermet fabrication. Higher porosity is achieved by adding pore formers, such as graphite, carbon black, or corn starch, in the early fabrication steps which burn out of the structure during sintering in air, leaving pores for gas diffusion. In a thorough parameter investigation [80] of a YSZ-based cell, the Ni-YSZ cermet anode porosity was varied between 32% and 76%, in four test cells, by controlling the amount of pore former added to the precursor powders. With other parameters held constant, the peak power density varied from ~0.72W/cm^2 for a cell with anode porosity of 32% to ~1.55W/cm^2 for a cell with anode porosity of 57%; the increase in porosity significantly enhanced the performance. Considerable anode concentration polarization in the 32% porosity Ni-YSZ anode limited the maximum current density at high hydrogen partial pressures due to limited gas diffusion [80]. This study, as well as others [79], require that pore formers be used in oxygen anion conducting SOFC anodes to increase cell performance. A convention of approximately 20 wt% pore former precursor for anode fabrication has been adopted.

Proton conducting SOFCs differ from oxygen anion conducting SOFCs by where the products of the overall fuel cell reaction are formed. In oxygen anion conducting SOFCs, water is formed at the anode, diluting the fuel and thus reducing the Nernst potential. In contrast, water develops at the cathode in proton conducting SOFCs and the fuel remains pure. During routine operation, excess air is present at the cathode, therefore water formation at the cathode in proton conducting SOFCs has a minimal effect on cell voltage [6, 82]. Furthermore, in proton conducting SOFCs, fuel is the only gas diffusing through the anode, no water is present. In the proton conducting SOFC anode, less porosity is needed when compared to oxygen anion conducting SOFCs. By decreasing anode porosity, the volume fraction of active material in the

anode increases, which can increase the active area for fuel cell reactions and lead to increased performance.

A recent study [75] revealed the unique microstructure that is formed when no pore formers are used in the nickel cermet anode fabrication process using the commonly studied mixed oxygen anion, electronic, and proton conducting oxide, $BaZr_{0.6}Ce_{0.2}Y_{0.2}O_{3-\delta}$. However, the material was not tested in an electrochemical device and the electrochemical properties of the microstructure were not studied. A study of correlation between microstructure and electrochemical performance in proton conducting anode supported SOFCs is lacking in the literature.

In this work, the effect of anode microstructure on the performance of proton conducting SOFCs based on $BaZr_{0.1}Ce_{0.7}Y_{0.1}Yb_{0.1}O_{3-\delta}$ (BZCYYb) is investigated. Cells with Ni-BZCYYb cermet anodes of varying porosity were fabricated and tested. High performance is observed in the SOFCs with anodes of low porosity. This is in stark contrast to the conventional anode optimization trend for YSZ-based, oxygen anion conducting SOFCs. This work provides a new understanding for the rational development of high performance, intermediate temperature SOFCs based on proton-conducting electrolytes.

5.2. Experimental

5.2.1 Sample Preparation

The cermet anode was prepared by mixing 65wt% nickel oxide (Alfa Aesar, stock #45094, NiO) and 35 wt% $BaZr_{0.1}Ce_{0.7}Y_{0.1}Yb_{0.1}O_{3-\delta}$ powders (described in chapter 3), ball milling in ethanol for 24 hours, to achieve a homogeneous mixture, followed by drying. Three separate samples, containing 0 wt%, 10 wt% and 20 wt% corn starch pore former, were prepared

from the NiO-$BaZr_{0.1}Ce_{0.7}Y_{0.1}Yb_{0.1}O_{3-\delta}$ mixture. These samples are labeled Ni-BZCYYb-0, Ni-BZCYYb-10, Ni-BZCYYb-20.

Button cells were fabricated by uniaxial pressing ($18x10^3$ psi) anode supports (d=13mm) with thickness of ~1mm. The anode supports were fired at 800°C for 2h to remove pore formers and binders. The sample containing no pore former (Ni-BZCYYb-0) was also fired at 800°C for consistency, although it was not necessary to remove pore former. $BaZr_{0.1}Ce_{0.7}Y_{0.1}Yb_{0.1}O_{3-\delta}$ electrolyte slurry [83] was drop coated onto the anode supports and co-fired at 1400°C for 5h to achieve a high density electrolyte. The final electrolyte thickness was ~20μm. For the anode microstructure specific tests, the anodes were fired under the same conditions but without electrolyte. For full cell preparation, $La_{0.6}Sr_{0.4}Co_{0.2}Fe_{0.8}$ $O_{3-\delta}$ (LSCF, Fuel Cell Materials, Lot #5C030)-BZCYYb (7:3 weight ratio) powders were mixed with V-006 and acetone to form a cathode slurry, which was brush-painted on the BZCYYb electrolyte, followed by firing at 800°C for 2h to form a porous LSCF-BZCYYb cathode on a BZCYYb electrolyte supported cell. Silver wire and silver paste (Heareus) was used for current collection.

Bar samples (16mm x 3.3mm x 2.15mm) were prepared by uniaxial pressing of the NiO-BZCYYb-0, NiO-BZCYYb-10, and NiO-BZCYYb-20 anode powders for electrical conductivity measurements. The bars were sintered at 1400°C for 5h to burn out the pore forming additives. Gold wires were attached to the samples for testing.

Exposure to hydrogen at high temperatures to reduce NiO to Ni metal is the last step in fabrication of a porous cermet anode with the final microstructure. Samples used for electrical conductivity tests and BET surface area measurements were first reduced in 100% H_2 at 750°C

for 2-4 hours to achieve the cermet anode structure similar to that produced under true fuel cell conditions.

5.2.2. Characterization

The microstructure of the cermet Ni-BZCYYb anode supported cell was examined using a thermally assisted field emission scanning electron microscope (SEM, LEO 1530). BET surface area per weight (m^2/g) was measured using a Micromeritics Tristar II 3020 surface area analyzer (nitrogen). The electrical conductivity was calculated from resistance measurements on Ni-BZCYYb bar samples collected using the 4 probe method.

The Archimedes method, using water as fluid, was used to measure porosity. Samples were dried overnight and weighed to determine the dry weight. To increase water infiltration for the submerged and wet sample measurements, samples were held under vacuum for 2h before water was added. Surface area per volume (mm^2/mm^3) was calculated using the density calculations taken from data collected by the Archimedes method.

For button cell SOFC testing, the cell was sealed (Ceramabond 552, Aremco) onto an alumina fuel cell testing fixture, with humidified hydrogen as fuel and ambient air as oxidant at 650^{o}C, 700^{o}C, and 750^{o}C. The cell was tested using an Arbin multi-channel electrochemical testing system (MSTAT).

5.3 Results

5.3.1. Ni-BZCYYb Anode Microstructure

Porosity in the Ni-BZCYYb anodes increased, as expected, with the amount of pore former added to the precursor powders (Table 5). However, the surface area per volume decreased with porosity.

Table 5: Ni-BZCYYb cermet anode porosity and surface area (mm^2/mm^3) based on pore former content

Cermet Precursor Pore Former (wt%)	Ni-BZCYYb Anode Porosity	Surface Area (mm^2/mm^3)
0	0.37	2430
10	0.42	2000
20	0.50	1428

Though counterintuitive, the increased specific surface area, measured by BET and observed by SEM (Figure 27), is explained by the unique microstructures created by the reduction of NiO to Ni(metal) in the Ni-BZCYYb anodes.

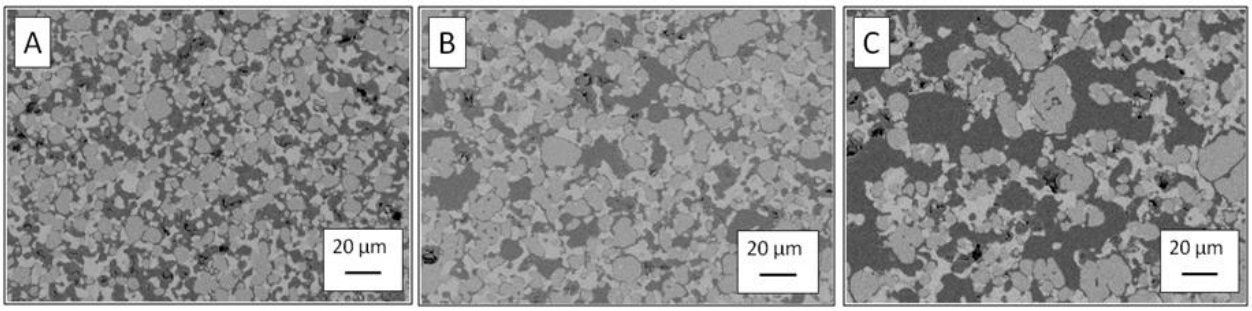

Figure 27: SEM (backscattered electron) images (Light-gray=BZCYYb, Mid-gray=Ni (metal), Dark-gray/Black=Epoxy) of A.) Ni-BZCYYb-0, B.) Ni-BZCYYb-10, and C.)Ni-BZCYYb-20 anode microstructures.

Porosity is formed in the anode in two ways: first by the burning of pore forming additives during firing, leaving large, round pores, and second by the reduction of NiO to Ni upon exposure to a fuel at high temperatures, leaving long channels of pores between the Ni(metal) phase and the BZCYYb phase. Pore forming additives can create large pores, beneficial to water vapor transport through the anode of an oxygen anion conducting SOFC,

however, the round “pockets” of pores have low surface area to volume ratio. Porosity due to pore former burnout is created during the sintering step of the fabrication process. Some pores are lost in the sintering step due to shrinkage. Next, during the reduction of NiO to Ni(metal), a 41.2% reduction in volume of the NiO phase occurs[19]. As oxygen diffuses out of the NiO during the reduction, the nickel particles shrink and “pull-away” from the surrounding BZCYYb framework. Narrow channels form between the phases, creating long, narrow pores with high surface area to volume ratio. If pore forming additives are used, both mechanisms create pores in the sample. In the Ni-BZCYYb-0 sample (without pore former), only NiO reduction to Ni(metal) contributed to the anode porosity.

Because pore formation in the NiO reduction occurs after the pore forming additive burn-out (corn starch), the pores formed in the NiO reduction are affected by the pores formed from the pore forming additive (corn starch) burnout. The large, round “pockets” of pores formed by the corn starch allow the oxygen to easily diffuse out of the NiO particles and the anode. However, in the sample with no pores before reduction, the oxygen must take a tortuous path to diffuse out of the NiO particle and the anode. This results in more intricate microstructures on the surface of the nickel particles [19] and more channels of pores surrounding the Ni(metal) particles.

High surface area per volume is important in anodes for SOFCs. More surface area provides more open sites for anode reactions and can lead to increased length of triple phase boundaries, although quantification of TPB length is difficult and was not attempted in this study. As seen in Table 5, the Ni-BZCYYb-0 anode (37% porosity) developed the largest surface area per volume.

Backscattered electron SEM images of each of the anode samples are shown in Figure 27. The samples were filled with epoxy and polished to determine the porosity on one focal plane. In the images, the dark-gray phase is epoxy, the light-gray phase is BZCYYb, and the mid-gray phase is Ni(metal). Dark, irregular patches in the images are caused by epoxy pull-out during polishing. Narrow channels between the Ni (metal) phase and the BZCYYb phase can be clearly seen. Also, absent from the Ni-BZCYYb-0 sample, but present in the Ni-BZCYYb-10 and Ni-BZCYYb-20 samples, is large "pockets" of pores. These large, round pores increase porosity but significantly decrease surface area per volume, leading to fewer sites for fuel oxidation.

5.3.2. Ni-BZCYYb Cermet Anode Electrical Conductivity

Ni-BZCYYb anode electrical conductivity was measured using the 4 probe method (Figure 28). For optimal anode performance, the nickel phase must provide a contiguous pathway throughout the anode to remove electrons from the hydrogen oxidation process at the TPBs. As porosity increases, the nickel particles are less interconnected, decreasing the electrical conductivity. The conductivity in the anodes of 37% and 42% porosity are sufficient for high anode performance and are also significantly higher than that of the anode with 50% porosity.

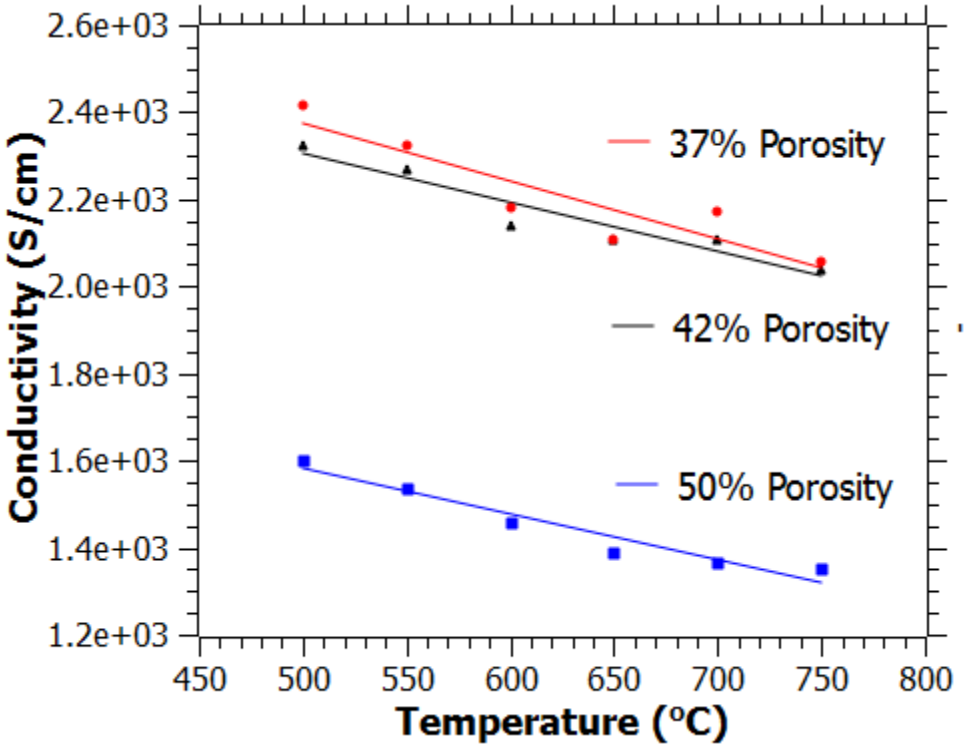

Figure 28: Electrical conductivity of Ni-BZCYYb-0 (37% porosity), Ni-BZCYYb-10 (42% Porosity), and Ni-BZCYYb-20 (50% Porosity) under reducing atmosphere measured using a 4-probe technique.

The percolation threshold of nickel (metal) in Ni-YSZ cermet anodes is approximately 35% [84]. The electrical conductivity data in this work suggests that the nickel (metal) content in the Ni-BZCYYb cermet anodes with 37% and 42% porosity is above the percolation threshold due to high volume fraction of nickel (metal). However, the significant drop in conductivity of the Ni-BZCYYb-20 sample implies that the nickel (metal) content is in the region of the percolation threshold.

5.3.3. SOFC Performance

Figure 29A reveals a cross-sectional view of a test cell with a configuration of Ni-BZCYYb-0/BZCYYb/LSCF-BZCYYb. All the Ni-BZCYYb anode-supported cells have a dense

electrolyte of ~20 μm thick. The Ni-BZCYYb-0 anode microstructure, after reduction, is represented in Figure 29B.

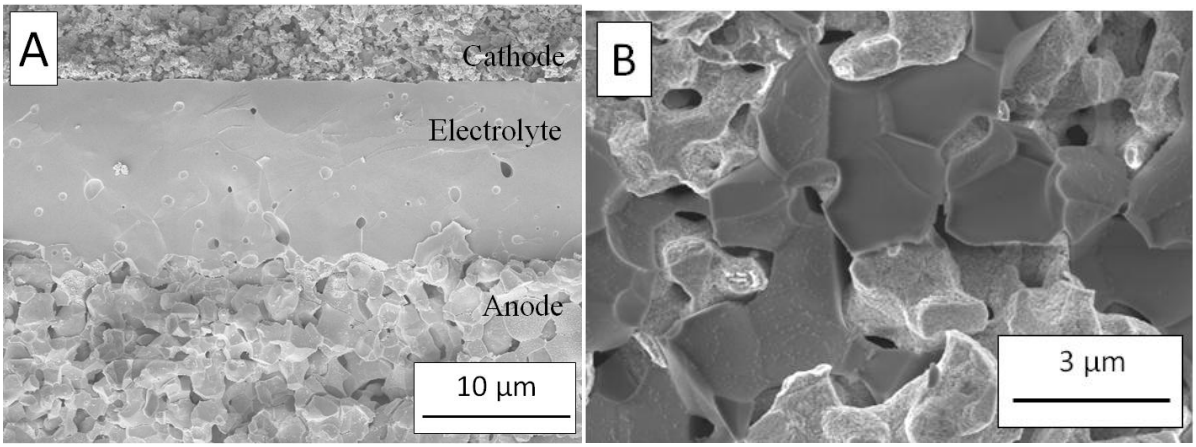

Figure 29: A.) SEM (secondary electron) images of a typical cross-sectional view of an anode-supported test cell with a configuration of Ni-BZCYYb/BZCYYb/LSCF-BZCYYb (electrolyte thickness = ~20 μm for all test cells) and, B.) Ni-BZCYYb-0 anode microstructure after reduction in hydrogen at 750^{o}C for 2 hours.

Figure 30 shows some typical performance data at 650^{o}C, 700^{o}C, and 750^{o}C for three cells based on BZCYYb with anodes of different porosity and microstructure: (A) a Ni-BZCYYb-0 anode (without pore former), (B) a Ni-BZCYYb-10 anode (with 10% pore former), and (C) a Ni-BZCYYb-20 anode (with 20% pore former). The detailed microscopic features of the anodes with different amount of pore former are shown in Figure 27. The highest performance is observed in the cell with the Ni-BZCYYb-0 anode (without pore former, 37% porosity). Peak power densities of 1.20W/cm^2, 1.02W/cm^2, and .73W/cm^2 were observed at 750^{o}C, 700^{o}C, and 650^{o}C, respectively. At 750^{o}C, the cell with the Ni-BZCYYb-0 anode outperformed the one with the Ni-BZCYYb-10 anode by 20% and the one with the Ni-BZCYYb-20 anode cell by 30%. The peak power densities observed under different conditions are summarized in Figure 30D.

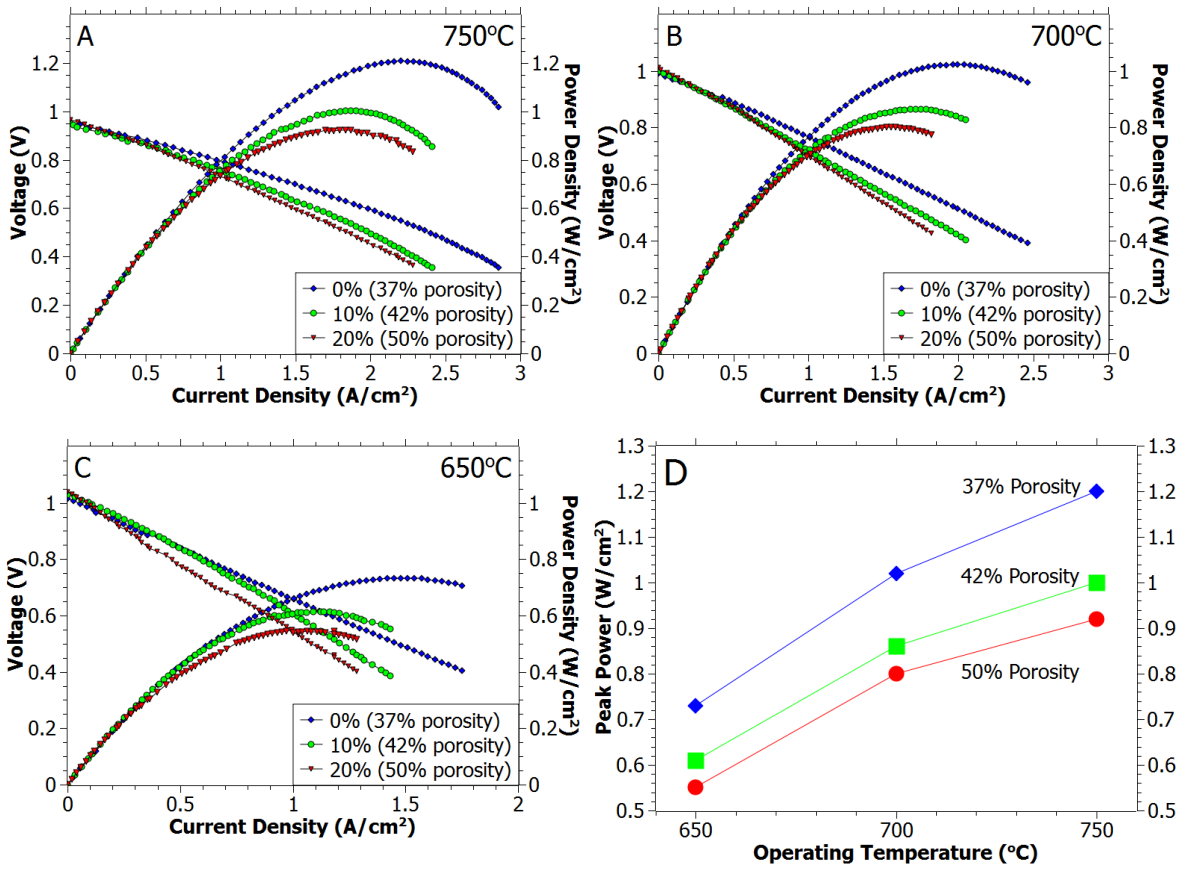

Figure 30: Typical I-V curves and calculated power densities for Ni-BZCYYb-0/BZCYYb/LSCF-BZCYYb, Ni-BZCYYb-10/BZCYYb/LSCF-BZCYYb, and Ni-BZCYYb-20/BZCYYb/LSCF-BZCYYb cells at A.) 750°C, B.) 700°C, and C.) 650°C; and D.) A summary of the peak power densities of each cell at all testing temperatures

The straightness of the I-V curves suggest that concentration polarization in these cells is relatively small, an indication of sufficient porosity for gas transport of fuel and reaction products. The electrical conductivity data suggests that increased contiguity of the nickel phase in the 37% porosity sample does not lead to a significant improvement in electrical conductivity over the 42% porosity sample. Therefore, the small improvement in electrical conductivity may have little impact on anode performance. Accordingly, the increased performance in the cell with the anode fabricated without the use of pore former is attributed primarily to the unique microstructure which forms during NiO reduction. It appears that the small pores derived from

reduction of NiO to Ni (metal) alone would be sufficient for hydrogen transport through the anode for proton-conducting SOFCs.

5.4 Discussion

Because water is formed at the cathode side for a proton conducting SOFC, the anode for such a cell requires less porosity than oxygen anion conducting SOFCs, where the water is formed at the anode side. The reduction of NiO to Ni(metal) alone produces sufficient porosity for fast fuel diffusion to the triple phase boundary reaction sites in the anode. Lowering the porosity increases active material in the anode and by not using pore forming additives, unique microstructures form in the anode which leads to enhanced anode activity and improved SOFC performance. The microstructure formed by Ni(metal) "pull-away" from the ion-conducting phase during reduction forms narrow channels of pores instead of large, round pores left by pore forming additives. The channel pores increase the surface area (and TPBs) per unit volume in the anode which leads to increased activity for SOFC reactions. The high specific surface area, low porosity anode was tested alongside anodes fabricated using pore forming additives and a large increase in performance was observed at temperature ranges of $650^{o}C$ – $750^{o}C$. Peak power densities of $0.73 W/cm^2$ and $1.2 W/cm^2$ were observed at $650^{o}C$ and $750^{o}C$, respectively, for proton conducting SOFCs based on low porosity, high specific surface area nickel-cermet anodes.

CHAPTER 6

CONCLUSIONS AND FUTURE DIRECTION

SEM characterization revealed the microstructure of the pure BZCYYb and the NiO-BZCYYb mixture after sintering. The NiO addition to BZCYYb significantly improved the sinterability of the BZCYYb material. HT-XRD revealed peak splitting of the characteristic perovskite peaks in the pure BZCYYb pellets. While the exact structure was not refined, the changes in peaks with temperature were attributed to changes in the symmetry of the structure with temperature. Structural phase changes in similar $BaCeO_3$-based systems reported in the literature were studied and their conclusions were used to discuss our results.

Further investigation of the BZCYYb system should correlate the exact structural transition temperatures to the BZCYYb electrical conductivity and transport data. Because symmetry affects the transport in the $BaCeO_3$-based systems, it is thought that the use of dopants to intentionally change the symmetry can be used to tailor the electrical properties at specific temperatures for use in electrochemical devices.

A report by Knight [64] on the structural phase transitions in the $BaCeO_3$-based systems articulates the inadequacy of laboratory scale XRD for the characterization of the exact structure and transformation temperatures in the perovskite oxides. In X-ray diffraction, atomic number is directly related to the scattering cross-section, which makes the identification of light atoms much more difficult, especially when the cations have very high atomic number, as is the case in $BaCeO_3$. However, in neutron diffraction, the scattering factor does not have the same relationship to the atomic number and fortunately, oxygen has a higher scattering factor than the other 2 elements. High energy synchrotron XRD photons allow for high resolution of the XRD

peaks which can be used with neutron diffraction to determine the transformation temperatures. Therefore, because of the sensitivity to oxygen and the specific changes that occur in the neutron diffraction pattern as a result of the BO_6 octahedra tilting [64], and the high resolution of synchrotron XRD future studies should include neutron diffraction analysis and synchrotron XRD.

The research has determined the conductivity and transport numbers of the BZCYYb system under conditions relevant to IT-SOFCs. The BZCYYb is a mixed proton, oxygen anion, and electronic conductor depending on the atmosphere and temperature. Under IT-SOFC cathode conditions, the BZCYYb material is a majority oxygen anion conductor, but also has significant proton conduction (at 600^{o}C t_{H^+}= 0.3). Under IT-SOFC anode conditions, the BZCYYb material is a majority proton conductor (at 600^{o}C t_{H^+}= 0.87). The conductivity data revealed lower activation energy for protonic transport than for oxygen anion transport, as reported in the literature. The conductivity of the BZCYYb in O_2/H_2O atmosphere is highest above 600^{o}C and the conductivity in H_2/H_2O atmosphere is highest below 600^{o}C due to the charge carrier transition.

The electrical conductivity and transport numbers should be determined in the NiO-BZCYYb mixture due to its existence in the BZCYYb electrolyte fabricated on the Ni-BZCYYb anode. Also, synchrotron XRD and neutron diffraction should be used to determine if the NiO acts to stabilize the high symmetry perovskite phases of the BZCYYb at RT.

In addition to the concentration cell – OCV method, another method to determine the transference numbers under real fuel cell conditions can be used. By monitoring the water vapor evolution rate at the electrodes of the cell while a D.C. bias is applied, the transference numbers can be determined. The water vapor, formed at the cathode and anode under fuel cell operation,

is directly proportional to the number of oxygen vacancies and protons, respectively, transported through the electrolyte as seen in equation 16. Iwahara [23] has demonstrated the use of a hygrometer to determine the water vapor content at the electrodes. The amount of water formed at each electrode is directly related to the current that is drawn from the cell. Small, button-cell electrodes can only support a small current which means that the water formed at the electrodes will be very small [70]. The measurement of water vapor evolution has been used to characterize $BaCe_{0.9}Sm_{0.1}O_{3-\alpha}$ under real fuel cell conditions [24]. While this method will give actual transference numbers under real fuel cell conditions, several experimental difficulties exist. As mentioned before, the best commercial sealant material does not perfectly seal the fuel cell to the testing fixture. Porosity in the sealant material allows hydrogen to diffuse to the oxygen side and oxygen to the hydrogen side. This will increase the water formation and skew the results. SOFC sealant materials are widely researched and improvements in high temperature sealant materials will lead to more accurate results and make this technique more feasible. Also the small amount of water formed by test cells requires a highly sensitive hygrometer or perfect water collection system to precisely determine the water formation at each electrode. The electronic transport cannot be determined by this method, however the difference in theoretical and measured cell OCV can be used to determine the electronic transport. Transport numbers of the BZCYYb system, determined by measuring the water formation at each electrode, should be determined and compared to the transference numbers determined by the concentration cell - OCV method in this work.

Significant protonic conduction in the BZCYYb material leads to water formation at the cathode side of the IT-SOFC which decreases the required porosity in the anode of the cell. In the cells fabricated in this study, adequate porosity is achieved by the reduction of NiO to

Ni(metal) alone and pore formers are not needed. A unique microstructure forms in the anode when no pore formers are used, and a significant increase in performance is observed. The cell based on the Ni-BZCYYb anode with the lowest porosity achieved the highest performance. In the future, this work should be applied to similar proton conducting IT-SOFC systems to test the transferability of the concept. From our results and conclusions, we believe significant performance enhancements in other proton conducting IT-SOFC systems can be realized.

REFERENCES

1. Friedli, H., et al., *Ice Core Record of the C-13/C-12 Ratio of Atmospheric Co2 in the Past 2 Centuries.* Nature, 1986. **324**(6094): p. 237-238.
2. Abruna, H.D., J.B. Goodenough, and M. Buchanan, *ANYL 28-Summary overview of basic research needs for electrical energy storage.* Abstracts of Papers of the American Chemical Society, 2007. **234**.
3. Song, C.S., *Fuel processing for low-temperature and high-temperature fuel cells - Challenges, and opportunities for sustainable development in the 21st century.* Catalysis Today, 2002. **77**(1-2): p. 17-49.
4. Liang, Y.Y., et al., *For the Bright Future-Bulk Heterojunction Polymer Solar Cells with Power Conversion Efficiency of 7.4%.* Advanced Materials, 2010. **22**(20): p. E135-+.
5. Razykov, T.M., et al., *Solar photovoltaic electricity: Current status and future prospects.* Solar Energy, 2011. **85**(8): p. 1580-1608.
6. Singhal, S.C. and K. Kendall, *High Temperature Solid Oxide Fuel Cells: Fundamentals, Design and Applications*, ed. S.C. Singhal, Kendall, Kevin. 2003, Amsterdam: Elsevier.
7. Carrette, L., K.A. Friedrich, and U. Stimming, *Fuel Cells - Fundamentals and Applications.* Fuel Cells, 2001. **1**(1): p. 5-39.
8. *The Fuel Cell Today Industry Review 2011*. 2011, Johnson Matthey PLC: Royston. p. 2-36.
9. Minh, N.Q., *Technological Status of Nickel-Oxide Cathodes in Molten Carbonate Fuel-Cells - a Review.* Journal of Power Sources, 1988. **24**(1): p. 1-19.
10. Minh, N.Q., *Ceramic Fuel-Cells.* Journal of the American Ceramic Society, 1993. **76**(3): p. 563-588.
11. Steele, B.C.H. and A. Heinzel, *Materials for fuel-cell technologies.* Nature, 2001. **414**(6861): p. 345-352.
12. Singhal, S.C., *Solid oxide fuel cells for stationary, mobile, and military applications.* Solid State Ionics, 2002. **152**: p. 405-410.
13. Liu, M., et al., *Rational SOFC material design: new advances and tools.* Materials Today, 2011. **14**(11): p. 534-546.
14. Liu, M., et al., *Direct octane fuel cells: A promising power for transportation.* Nano Energy, 2012. **1**(3): p. 448-455.
15. Yang, L., et al., *Promotion of water-mediated carbon removal by nanostructured barium oxide/nickel interfaces in solid oxide fuel cells.* Nature Communications, 2011. **2**: p. 357.
16. Yang, L., et al., *Enhanced Sulfur and Coking Tolerance of a Mixed Ion Conductor for SOFCs: BaZr0.1Ce0.7Y0.2-xYbxO3-delta.* Science, 2009. **326**(5949): p. 126-129.
17. Singhal, S.C., *Advances in solid oxide fuel cell technology.* Solid State Ionics, 2000. **135**(1-4): p. 305-313.
18. Zuo, C.D., et al., *Ba(Zr0.1Ce0.7Y0.2)O3-delta as an electrolyte for low-temperature solid-oxide fuel cells.* Advanced Materials, 2006. **18**(24): p. 3318-+.
19. Kreuer, K.D., *Aspects of the formation and mobility of protonic charge carriers and the stability of perovskite-type oxides.* Solid State Ionics, 1999. **125**(1-4): p. 285-302.
20. Manning, P.S., et al., *The kinetics of oxygen transport in 9.5 mol % single crystal yttria stabilised zirconia.* Solid State Ionics, 1997. **100**(1-2): p. 1-10.
21. Fabbri, E., D. Pergolesi, and E. Traversa, *Electrode materials: a challenge for the exploitation of protonic solid oxide fuel cells.* Science and Technology of Advanced Materials, 2010. **11**(4).
22. Zuo, C., et al., *$Ba(Zr_{0.1}Ce_{0.7}Y_{0.2})O_3$ as Electrolyte for Low-temperature SOFCs.* Advanced Materials, 2006. **18**: p. 3318-3320.

23. Iwahara, H., T. Yajima, and H. Ushida, *Effect of Ionic-Radii of Dopants on Mixed Ionic-Conduction (H++O2-) in Baceo3-Based Electrolytes.* Solid State Ionics, 1994. **70**: p. 267-271.
24. Iwahara, H., et al., *Performance of Solid Oxide Fuel-Cell Using Proton and Oxide-Ion Mixed Conductors Based on Bace1-Xsmxo3-Alpha.* Journal of The Electrochemical Society, 1993. **140**(6): p. 1687-1691.
25. Bonanos, N., K.S. Knight, and B. Ellis, *Perovskite Solid Electrolytes - Structure, Transport-Properties and Fuel-Cell Applications.* Solid State Ionics, 1995. **79**: p. 161-170.
26. Zhou, X.L., et al., *Ionic conductivity, sintering and thermal expansion behaviors of mixed ion conductor BaZr0.1Ce0.7Y0.1Yb0.1O3-delta prepared by ethylene diamine tetraacetic acid assisted glycine nitrate process.* Journal of Power Sources, 2011. **196**(11): p. 5000-5006.
27. Mobius, H.H., *On the history of solid electrolyte fuel cells.* Journal of Solid State Electrochemistry, 1997. **1**(1): p. 2-16.
28. Bard, A.J. and L.R. Faulkner, *Electrochemical Methods: Fundamentals and Applications*. 2nd ed. 2001, Hoboken, NJ: Wiley.
29. Liu, M. and H. Hu, *Effect of interfacial resistance on determination of transport properties of mixed conducting electrolytes.* Journal of The Electrochemical Society, 1996. **143**(6): p. L109-L112.
30. Kiukkola, K. and C. Wagner, *Measurements on Galvanic Cells Involving Solid Electrolytes.* Journal of The Electrochemical Society, 1957. **104**(6): p. 379-387.
31. Zhu, Z.W., et al., *Synthesis and hydrogen permeation of Ni-Ba(Zr0.1Ce0.7Y0.2) O3-delta metal-ceramic asymmetric membranes.* International Journal of Hydrogen Energy, 2011. **36**(10): p. 6337-6342.
32. Zuo, C., et al., *Composite Ni-Ba(Zr0.1Ce0.7Y0.2)O3 membrane for hydrogen separation.* Journal of Power Sources, 2006. **159**(2): p. 1291-1295.
33. Iwahara, H., *Technological Challenges in the Application of Proton Conducting Ceramics.* Solid State Ionics, 1995. **77**: p. 289-298.
34. *Perovskite oxide for solid oxide fuel cells*. Fuel cells and hydrogen energy. 2009, New York: Springer.
35. Iwahara, H., et al., *Proton Conduction in Sintered Oxides and Its Application to Steam Electrolysis for Hydrogen-Production.* Solid State Ionics, 1981. **3-4**(Aug): p. 359-363.
36. Ricote, S., et al., *Conductivity, transport number measurements and hydration thermodynamics of BaCe0.2Zr0.7Y(0.1-xi)Ni xi O(3-delta).* Solid State Ionics, 2011. **185**(1): p. 11-17.
37. Iwahara, H., et al., *Proton Conduction in Sintered Oxides Based on Baceo3.* Journal of The Electrochemical Society, 1988. **135**(2): p. 529-533.
38. Paria, M.K. and H.S. Maiti, *Electrical-Conduction in Barium Cerate Doped with La2o3, Nd2o3, Ho2o3.* Solid State Ionics, 1984. **13**(4): p. 285-292.
39. Bonanos, N., B. Ellis, and M.N. Mahmood, *Construction and Operation of Fuel-Cells Based on the Solid Electrolyte Baceo3-Gd.* Solid State Ionics, 1991. **44**(3-4): p. 305-311.
40. Bonanos, N., *Transport Study of the Solid-Electrolyte Bace0.9gd0.1o2.95 at High-Temperatures.* Journal of Physics and Chemistry of Solids, 1993. **54**(7): p. 867-870.
41. Taniguchi, N., et al., *Proton Conductive Properties of Gadolinium-Doped Barium Cerates at High-Temperatures.* Solid State Ionics, 1992. **53**: p. 998-1003.
42. Amsif, M., et al., *Influence of rare-earth doping on the microstructure and conductivity of BaCe(0.9)Ln(01)O(3-delta) proton conductors.* Journal of Power Sources, 2011. **196**(7): p. 3461-3469.
43. Kreuer, K.D., *Proton-conducting oxides.* Annual Review of Materials Research, 2003. **33**: p. 333-359.

44. Wu, J., et al., *Atomistic study of doped BaCeO3: Dopant site-selectivity and cation nonstoichiometry.* Chemistry of Materials, 2005. **17**(4): p. 846-851.
45. Bonanos, N., et al., *Ionic-Conductivity of Gadolinium-Doped Barium Cerate Perovskites.* Solid State Ionics, 1989. **35**(1-2): p. 179-188.
46. Stevenson, D.A., et al., *Characterization of Gd, Yb and Nd Doped Barium Cerates as Proton Conductors.* Solid State Ionics, 1993. **62**(3-4): p. 279-285.
47. Giannici, F., et al., *Local environment of Barium, Cerium and Yttrium in BaCe(1-x)Y(x)O(3-delta) ceramic protonic conductors.* Solid State Ionics, 2007. **178**(7-10): p. 587-591.
48. Zhang, C.J., H.L. Zhao, and S.Y. Zhai, *Electrical conduction behavior of proton conductor BaCe(1-x)Sm(x)O(3-delta) in the intermediate temperature range.* International Journal of Hydrogen Energy, 2011. **36**(5): p. 3649-3657.
49. Kruth, A., et al., *Anomalous variations of unit cell parameters with composition in proton conducting, ACeO(3)-type perovskite solid solutions.* Solid State Ionics, 2005. **176**(7-8): p. 703-712.
50. Pergolesi, D., et al., *High proton conduction in grain-boundary-free yttrium-doped barium zirconate films grown by pulsed laser deposition.* Nature Materials, 2010. **9**(10): p. 846-852.
51. Katahira, K., et al., *Protonic conduction in Zr-substituted BaCeO3.* Solid State Ionics, 2000. **138**(1-2): p. 91-98.
52. Liu, M., *Development of Novel Electrolyte/Electrode Materials for a New Generation of Low-Temperature SOFCs*. 2011, Georgia Institute of Technology: Atlanta, GA.
53. Hibino, T., et al., *Proton conduction at the surface of Y-doped BaCeO3 and its application to an air/fuel sensor.* Journal of Materials Science, 2004. **39**(7): p. 2493-2497.
54. Su, X.T., et al., *Effect of co-dopant addition on the properties of yttrium and neodymium doped barium cerate electrolyte.* Solid State Ionics, 2006. **177**(11-12): p. 1041-1045.
55. Rahaman, M.N., *Ceramic processing*. 2007, Boca Raton, FL: CRC/Taylor & Francis. 473 p.
56. Liu, Y., et al., *Enhanced sinterability of BaZr(0.1)Ce(0.7)Y(0.1)Yb(0.1)O(3-delta) by addition of nickel oxide.* Journal of Power Sources, 2011. **196**(23): p. 9980-9984.
57. Tong, J.H., et al., *Solid-state reactive sintering mechanism for large-grained yttrium-doped barium zirconate proton conducting ceramics.* Journal of Materials Chemistry, 2010. **20**(30): p. 6333-6341.
58. Haile, S.M. and K.H. Ryu, *Chemical stability and proton conductivity of doped BaCeO3-BaZrO3 solid solutions.* Solid State Ionics, 1999. **125**(1-4): p. 355-367.
59. Shima, D. and S.M. Haile, *The influence of cation non-stoichiometry on the properties of undoped and gadolinia-doped barium cerate.* Solid State Ionics, 1997. **97**(1-4): p. 443-455.
60. Subramaniyan, A., et al., *Sintering Studies on 20 mol% Yttrium-Doped Barium Cerate.* Journal of the American Ceramic Society, 2011. **94**(6): p. 1800-1804.
61. Malavasi, L., C. Ritter, and G. Chiodelli, *Correlation between thermal properties, electrical conductivity, and crystal structure in the BaCe0.80Y0.20O2.9 proton conductor.* Chemistry of Materials, 2008. **20**(6): p. 2343-2351.
62. Malavasi, L., et al., *Combined Neutron and Synchrotron X-ray Diffraction investigation of the BaCe0.85-xZrxY0.15O3-delta (0.1 <= x <= 0.4) Proton Conductors.* Chemistry of Materials, 2011. **23**(5): p. 1323-1330.
63. Tu, C.S., et al., *Temperature-dependent structures of proton-conducting Ba(Zr0.8-xCexY0.2)O-2.9 ceramics by Raman scattering and x-ray diffraction.* Journal of Physics-Condensed Matter, 2012. **24**(15).
64. Knight, K.S., *Structural phase transitions, oxygen vacancy ordering and protonation in doped BaCeO3: results from time-of-flight neutron powder diffraction investigations.* Solid State Ionics, 2001. **145**(1-4): p. 275-294.

65. Cordero, F., et al., *Effect of doping and oxygen vacancies on the octahedral tilt transitions in the BaCeO3 perovskite.* Physical Review B, 2010. **82**(10).
66. Yajima, T., H. Iwahara, and H. Uchida, *Protonic and Oxide Ionic-Conduction in Baceo3-Based Ceramics - Effect of Partial Substitution for Ba in Bace0.9nd0.1o3-Alpha with Ca.* Solid State Ionics, 1991. **47**(1-2): p. 117-124.
67. Bonanos, N. and F.W. Poulsen, *Considerations of defect equilibria in high temperature proton-conducting cerates.* Journal of Materials Chemistry, 1999. **9**(2): p. 431-434.
68. Wagner, C., *The theory of the warm-up process.* Zeitschrift Fur Physikalische Chemie-Abteilung B-Chemie Der Elementarprozesse Aufbau Der Materie, 1933. **21**(1/2): p. 25-41.
69. Norby, T. and P. Kofstad, *Proton and Native-Ion Conductivities in Y2o3 at High-Temperatures.* Solid State Ionics, 1986. **20**(3): p. 169-184.
70. Sutija, D.P., T. Norby, and P. Bjornbom, *Transport Number Determination by the Concentration-Cell Open-Circuit Voltage Method for Oxides with Mixed Electronic, Ionic and Protonic Conductivity.* Solid State Ionics, 1995. **77**: p. 167-174.
71. Iwahara, H., H. Uchida, and N. Maeda, *Studies on Solid Electrolyte Gas Cells with High-Temperature-Type Proton Conductor and Oxide Ion Conductor.* Solid State Ionics, 1983. **11**(2): p. 109-115.
72. Guan, J., et al., *Transport properties of $BaCe_{0.95}Y_{0.05}O_{3-\alpha}$ mixed conductors for hydrogen separation.* Solid State Ionics, 1997. **100**(1,2): p. 45-52.
73. P.J. Linstrom and W.G. Mallard, E., ed. *NIST Chemistry WebBook, NIST Standard Reference Database Number 69*. 2012, National Institute of Standards and Technology: Gaithersburg, MD.
74. Iwahara, H., H. Uchida, and S. Tanaka, *High-Temperature Type Proton Conductor Based on Srceo3 and Its Application to Solid Electrolyte Fuel-Cells.* Solid State Ionics, 1983. **9-10**(Dec): p. 1021-1025.
75. Coors, W.G. and A. Manerbino, *Characterization of composite cermet with 68 wt.% NiO and BaCe(0.2)Zr(0.6)Y(0.2)O(3-delta).* Journal of Membrane Science, 2011. **376**(1-2): p. 50-55.
76. Atkinson, A., et al., *Advanced anodes for high-temperature fuel cells.* Nature Materials, 2004. **3**(1): p. 17.
77. Zunic, M., et al., *Influence of the ratio between Ni and BaCe(0 9)Y(0 1)O(3-delta) on microstructural and electrical properties of proton conducting Ni-BaCe(0) (9)Y(0) (1)O(3-delta) anodes.* Journal of Alloys and Compounds, 2011. **509**(4): p. 1157-1162.
78. Bi, L., E. Fabbri, and E. Traversa, *Effect of anode functional layer on the performance of proton-conducting solid oxide fuel cells (SOFCs).* Electrochemistry Communications, 2012. **16**(1): p. 37-40.
79. Suzuki, T., et al., *Impact of Anode Microstructure on Solid Oxide Fuel Cells.* Science, 2009. **325**(5942): p. 852-855.
80. Zhao, F. and A.V. Virkar, *Dependence of polarization in anode-supported solid oxide fuel cells on various cell parameters.* Journal of Power Sources, 2005. **141**(1): p. 79-95.
81. Fergus, J.W., *Solid oxide fuel cells : materials properties and performance*. Green chemistry and chemical engineering. 2009, Boca Raton: CRC Press. 295 p.
82. Bonanos, N., *Transport-Properties and Conduction Mechanism in High-Temperature Protonic Conductors.* Solid State Ionics, 1992. **53**: p. 967-974.
83. Liu, M.F., et al., *High performance of anode supported BaZr(0.1)Ce(0.7)Y(0.2)O(3-delta)(BZCY) electrolyte cell for IT-SOFC.* International Journal of Hydrogen Energy, 2011. **36**(21): p. 13741-13745.
84. Lee, J.H., et al., *Quantitative analysis of microstructure and its related electrical property of SOFC anode, Ni-YSZ cermet.* Solid State Ionics, 2002. **148**(1-2): p. 15-26.

PUBLICATION

1. Rainwater, B., M.F. Liu, and M.L. Liu, *A more efficient anode for SOFCs based on proton conductors*, Journal of Power Sources, Under review.